**University of Bath**

# A Novel Approach to Leading-Edge Vortex Suppression

S. Bull, N. Chiereghin, D. J. Cleaver and I. Gursul

University of Bath, United Kingdom

## Abstract

A novel approach to reduce the peak lift and pitching moment on a plunging airfoil is investigated through force, moment, and velocity measurements. This approach, unlike previous investigations of delayed flow separation and leading-edge vortex suppression, uses forced separation through deployment of a mini-tab near the leading-edge. The device can be activated for short time intervals during a gust encounter or unsteady manoeuvre at the expense of short-duration drag increase. Depending on the frequency and the amplitude of the wing motion and the mean angle of attack, roll-up of vorticity and the formation of a vortex can be delayed or even prevented. This change in the vortex dynamics provides effective lift and moment alleviation for post-stall angles of attack and for low reduced frequencies. In contrast, at low angles of attack the separated shear layer may roll up for the manipulated flow, resulting in vortex shedding and lift and nose-down pitching moment increase. These two distinct flow regimes cause decreased or increased lift force, with the most effective frequencies scaling with the reduced frequency. In contrast, the borderline between the two regions scales with the Strouhal number based on amplitude, and in particular with the minimum effective angle of attack during the cycle. The transient response was studied by investigating impulsively started plunging oscillations. During the first cycle, lift reduction is achieved for all frequencies within the range tested.

**Nomenclature**

| | |
|---|---|
| *A* | peak-to-peak amplitude of plunging motion |
| $C_l$ | lift coefficient |
| $C_m$ | quarter-chord pitching moment coefficient |
| *c* | chord length |
| *f* | oscillation frequency |
| *H* | height of mini-tab |
| *h* | displacement of airfoil |
| *k* | reduced frequency, $\pi fc/U_\infty$ |
| *Re* | Reynolds number |
| $St_A$ | Strouhal number based on amplitude |
| *T* | period of motion |
| *t* | time |
| $U_\infty$ | freestream velocity |
| *V* | velocity magnitude |
| $V_{pl}$ | plunge velocity |
| $\alpha_{pl}$ | induced angle of attack due to motion |
| $\alpha_0$ | mean angle of attack |
| $\alpha_{eff}$ | total effective angle of attack |
| $\omega$ | spanwise vorticity |

## I.  Introduction

Leading-edge vortices (LEVs) form over wings in unsteady flows in many engineering applications including small unmanned vehicles, aircraft in gusts and manoeuvres, wind turbines and rotorcraft blades. Unsteady wing motion results in flow separation near the leading-edge, leading to roll-up of the shear layer vorticity into coherent LEVs. Leading-edge vortices, also known as "dynamic stall" vortices for pitching wings, and their effects on aerodynamic loads have been investigated extensively [1-4]. Dynamic stall vortices produce

extra lift, causing maximum lift excursions, as well as large variations in the pitching moment as the vortices convect towards the trailing-edge. Similarly, there is mean-lift enhancement for periodically plunging airfoils at post-stall angles of attack [5]. Recently it was shown [6] that this mean-lift enhancement is also possible at pre-stall angles of attack, as it may not be possible to avoid LEV formation and shedding. Lift increase has also been observed for the periodic oscillations of freestream velocity magnitude [7, 8] and for airfoil surging motion [9].

In most engineering applications, these large excursions in aerodynamic loads need to be controlled. Large mean-lift is desirable in flapping-wing applications, but it is usually necessary to limit the lift fluctuations. Other engineering applications where load alleviation is needed are high aspect-ratio wings - over rotorcraft blades during dynamic stall, on wind turbine blades in the presence of in-flow turbulence, or on aircraft wings due to unsteady manoeuvre or gust-induced flow separation. In these cases, increased lift as well as pitching/bending moment may need to be alleviated. Hence, the formation, strength and convection of the leading-edge vortices need to be controlled.

Previous dynamic stall control schemes rely on delay of the flow separation: leading-edge periodic blowing (with zero net mass flux) [10, 11], leading-edge suction [12], leading-edge plasma actuation [13], variable leading-edge curvature [14], rotating cylinder leading-edge [15] and slotted airfoils [16]. With rotorcraft applications in mind, previous methods were investigated in order to increase the maneuverability and agility, speed and payload. According to Corke and Thomas [3], the goals are to reduce blade pitching moments and to increase cycle-averaged lift. These imply that potential dynamic stall control schemes may need to be applied for long durations and many cycles.

This article, with fixed-wing applications in mind, investigates an entirely different approach in which the flow near the leading-edge is subjected to forced separation. It is shown that it is possible to prevent the roll-up of vorticity and formation of the leading-edge vortex, which in turn may alleviate the aerodynamic loads. The primary goal for the fixed wing applications is to reduce the maximum lift and associated bending moment. We also keep in mind that, for future applications, reduced frequencies for atmospheric turbulence during cruise can reach as high as $k \approx 1$ [17]. Current loads control technologies use ailerons and spoilers, which become ineffective at high gust frequency due to their large inertia. Therefore, highly responsive actuators are needed for gust load mitigation. This paper examines a small control surface, called the fence or mini-tab, which is placed normal to the airfoil surface (see Figure 1). Although the fence is static during the plunging motion in this study, we envision that future

3

developments will enable early detection of gusts (for example, LIDAR turbulence sensor [18]) and activation of the mini-tab before the gust interacts with the wing. As such small control surfaces will only be deployed for short intervals in realistic applications, the associated drag increase is not important when compared to the potential load alleviation for the wing. The most logical location for the mini-tab is near the leading-edge where the shear layer due to the separation is ejected into the flow. For stationary wings near stall, the mini-tab is also the most effective when placed near the leading-edge [17], which causes fully separated flow over the airfoil. However, the shear layer dynamics and vortex formation will be different in the case of unsteady wings for which unsteady lift will also depend on the leading-edge vortices.

The main objective of this article is to study the potential of lift and pitching moment suppression for a periodically plunging airfoil, when a mini-tab (or fence) is located near the leading-edge. Lift, pitching moment, and velocity measurements by Particle Image Velocimetry have been carried out in a water tunnel. It is shown that, depending on the wing kinematics (frequency and amplitude), the roll-up of vorticity and formation of the leading-edge vortex are suppressed. This alleviates the aerodynamic loads.

## II.  Methods and Techniques

The experiments comprise of an airfoil plunging normal to the freestream velocity with sinusoidal motion, as depicted by Figure 1a. The velocity of the plunging motion, $V_{pl}(t)$, induces an angle of attack, $\alpha_{pl}(t)$, which varies throughout the motion (Figure 1b) and creates the total effective angle of attack, $\alpha_{eff}(t) = \alpha_0 + \alpha_{pl}(t)$. Two airfoil geometries were considered: A NACA 0012, which serves as a baseline comparison, and a NACA 0012 with a mini-tab located near the leading on the upper surface, as shown in Figure 1c. A range of geometric angles of attack, $\alpha_0$, were tested to determine the mini-tab performance for symmetric (0°), pre-stall (3, 5, 7, 9°) and post-stall (11, 13, 15°) conditions. The test matrix for sinusoidal motion covered a range of reduced frequencies $k \leq 1.1$ for non-dimensional peak-to-peak amplitudes of $A/c$ = 0.05, 0.10, 0.20, 0.30 and 0.50.

### A. Experimental Setup

All experiments were conducted in the free-surface, closed-loop water tunnel facility at the University of Bath. This facility can provide a freestream velocity ranging from 0 to 0.5 m/s to a working section of 381 x 508 x 1530 mm with a freestream turbulence intensity less than 0.5% [19]. The Reynolds number based on the chord length is $Re$ = 20,000. The experimental

rig is situated on top of the water tunnel, see Figure 2, which positions the wing vertically in the test section. To enforce quasi-2D conditions a pair of splitter plates were used at the wing root and tip. To cover the hole in the root of the stationary plate for wing motion, a third moving splitter plate is fixed to the wing root and sits $0.02c$ under the stationary root plate in order to minimize any free-surface effects. For the wing-tip splitter plate there is a clearance of $0.02c$. The two wings consisted of a NACA 0012 airfoil profile of chord length 62.7 mm and a semi-aspect ratio of 5. These were manufactured from polyamide using selective laser sintering, sanded smooth and painted matt-black to reduce reflectivity. To provide a high spanwise stiffness, a 25 mm by 5 mm carbon fibre insert was slotted along the span at $x/c = 0.25$. One of the wings was printed with a small slot of 0.75 mm width on the upper at $x/c = 0.08$ to accommodate the mini-tab geometry. This consisted of a carbon fibre strip of $t = 0.75$ mm width that friction fits into the wing slot and protrudes normal to the upper surface at a height $H/c = 0.04$. This location of the mini-tab has been tested previously on a stationary airfoil [17].

A rotation stage is situated at the top of wing assembly and can set the geometric angle of attack with an accuracy of ±0.2°. This is then connected to the moving carriage through the torque sensor. The moving carriage is constrained to the plunging axis via four air bearings that provide frictionless motion whilst absorbing the bending and torque loads to leave just the lift component of force. Plunging motion is supplied by a Zaber LSQ150B-T3 translation stage powered by a stepper motion with an X-MCB1 controller. This can produce motion that follows the sinusoidal function with an accuracy of 2%:

$$h = A/2\cos(2\pi f t) \qquad (1)$$

**B. Force and Moment Measurements**

A Futek S-beam tension/compression load cell (FSH00103) is used to measure force in the plunging axis only, i.e. the lift component. This load cell acts as a link between the motion stage and the moving carriage (Figure 2a). The constraints imposed by the air bearing assembly enables a relatively sensitive force sensor to be used for dynamic measurements (as the large bending and torque loads are removed). For pitching moment measurements, a Futek reaction torque sensor (FSH03990) is situated between the wing and moving carriage and is aligned with the wing quarter-chord axis. A StrainSense 4807A accelerometer is also mounted to the moving carriage in order to remove the inertial forces from the lift and pitching moment signals. This was achieved by subtracting the product of the moving mass and instantaneous acceleration from the raw signal. To better isolate the aerodynamic component, the signals

5

were put through 3rd order Butterworth band-stop filters to remove the dominant structural frequencies of the wing and moving carriage. A Butterworth low pass filter was then applied at 30 Hz to remove the remaining high frequency noise. The periodic lift and pitching moment measurements are presented as a phase-average of 50 periods at a sample frequency of 2,000 times the plunging frequency. When the start-up transients are considered, the aerodynamic loads are presented as a single run with the same sample frequency. For static loads the measurements were acquired at 1 kHz for 40 seconds. The uncertainty in lift coefficient was estimated to be ±0.05 for the static cases and ±0.15 for the dynamic cases. The uncertainty in pitching moment coefficient was estimated to be ±0.005 for the static cases and ±0.015 for the dynamic cases.

## C. Particle Image Velocimetry Measurements

Two-dimensional Particle Image Velocimetry (PIV) measurements were taken at the mid-span plane and focussed on the upper surface of the airfoil, as shown in Figure 2a. The water was seeded with hollow glass spheres of 8 to 12μm that were illuminated with a New Wave Solo Nd:YAG 50 mJ laser. The PIV measurements were conducted with 4 MPixel and 8 MPixel cameras. All image pairs were processed with INSIGHT 4G using an interrogation window of 32 X 32 pixels with a grid overlap of 0.25, yielding a resolution from $0.010c$ to $0.014c$ depending on the camera. The uncertainty of velocity measurements is estimated as 2% of the freestream velocity. All PIV measurements are presented as the average of phase-locked image pairs. For the periodic motion 100 image pairs were used for phase-averaging, whereas for the start-up transients 30 image pairs were used.

## III. Results

### A. Stationary Airfoils

Figure 3a presents the static lift coefficient for the 'baseline' NACA 0012 and the 'control' NACA 0012 with mini-tab alongside relevant investigations of the NACA 0012 in literature at comparable Reynolds numbers. The lift coefficient of the baseline NACA 0012 shows excellent agreement with previous measurements taken at the University of Bath using both the current lift measurement system [6] and a binocular strain gauge configuration [20]. A substantial amount of non-linearity can be seen in the lift curve slope, which is characteristic of a NACA 0012 airfoil at low Reynolds numbers [21-23]. The observed plateau between $\alpha_0 = 0$ to $2^o$ is attributed to laminar separation of the boundary layer followed by an abrupt reattachment at around $3^o$ [22], causing the sharp increase in lift curve slope. As the angle of

attack increases the gradient begins to decrease, confirming the formation of a laminar separation bubble on the upper surface [23]. This is highlighted in our measurements shown in Figure 3c, where a closed region of separation can be observed at $\alpha_0 = 5^\circ$ on the baseline airfoil. Despite the agreement with literature at low to moderate angles of attack, differences begin to manifest beyond stall. It has been shown that at low Reynolds numbers $O(10^4)$ the lift curve is highly sensitive to both turbulence intensity and Reynolds number [22, 24]. Considering the static lift of the 'control' airfoil in Figure 3a, the mini-tab drastically reduces the lift across the majority of the $\alpha_0$ range. This is shown in Figure 3c as a result of forced flow separation at the mini-tab location, which extends further downstream [25]. At post-stall conditions the mini-tab becomes less effective as the baseline airfoil is also in a fully separated state.

In Figure 3b the static pitching moment for the baseline airfoil shows excellent agreement with Ohtake *et al.* [23] at a similar Reynolds number. The causes of the undulations is not fully understood, but is most likely related to the laminar boundary layer behaviour responsible for the non-linearity in the lift curve. The mini-tab suppresses the undulations in the pitching moment at positive, pre-stall angles of attack but leads to a more negative 'nose-down' value due to the separated flow. At post-stall angles the control airfoil exhibits a less negative, nose-down, pitching moment. Similar to the lift response, the pitching moment is less effected by the mini-tab at negative angles of attack.

## B. Oscillating Airfoils

The test matrix for dynamic loads measurements includes a wide range of reduced frequencies, amplitudes and geometric angles of attack. This is reduced to a single performance parameter for the lift, $\Delta C_l$, and pitching moment, $\Delta C_m$, which are defined below:

$$\Delta C_l = \max(C_{l,control}) - \max(C_{l,baseline}) \tag{2}$$

$$\Delta C_m = \max(|C_{m,control}|) - \max(|C_{m,baseline}|) \tag{3}$$

These definitions are illustrated in Figure 4a and Figure 4b which present the phase-averaged lift and pitching moment respectively at $\alpha_0 = 15^\circ$, $A/c = 0.5$, $k = 0.24$ for both the baseline and control airfoils. In this case the baseline airfoil displays a distinct peak in lift and nose-down pitching moment at $t/T = 0.23$ which corresponds to the formation and shedding of a coherent LEV, see Figure 4c. For the control case the mini-tab suppresses the formation of the LEV and therefore displays significantly reduced magnitudes of both peak lift and pitching moment.

Peak lift reduction and hence beneficial performance will occur when $\Delta C_l < 0$. For the pitching moment, $\Delta C_m$ is defined as the difference in maximum absolute phase-averaged pitching moment between the control and baseline airfoils, as shown in Figure 4b. Any large excursion in pitching moment regardless of its sign is undesirable, thus the absolute term in Equation 3.

The performance of the mini-tab with respect to lift, $\Delta C_l$, is shown in Figure 5 for the entire test matrix. For the symmetry case at $\alpha_0 = 0^o$, the lift performance is fairly insensitive to both reduced frequency and amplitude, residing primarily in the 'detrimental' region which is defined as $\Delta C_l > 0$, i.e. the mini-tab increases the change in peak lift due to the flow separation induced by the mini-tab. The value of $\Delta C_l$ remains close to the static performance of the mini-tab at $k = 0.0$ and only begins to deviate into the beneficial region from $k = 0.9$ to 1.1, depending on the amplitude. For the pre-stall angles of attack, $\alpha_0 = 3, 5, 7^o$, the lift change becomes more sensitive to $k$ and $A/c$. It consistently increases with $A/c$ at low reduced frequencies. For the stall angle $\alpha_0 = 9^o$ at the largest amplitude, $A/c = 0.5$, $\Delta C_l$ initially decreases at low $k$ before increasing so that the monotonic trend is lost. Superposed onto this general treand of increasing $\Delta C_l$ with $k$ and $A/c$ are maxima for pre-stall angles of attack. For $\alpha_0 = 5^o$ at $A/c = 0.5, 0.3, 0.2,$ 0.1, 0.05, these occur at $k = 0.4, 0.52, 0.52, 0.6$ and 0.8 respectively. These peaks at pre-stall angles of attack and how they scale with the main parameters will be discussed later. The curves for the highest amplitudes tend to converge towards $\Delta C_l = 0$ at high reduced frequencies indicating a reduced effect of the mini-tab in extreme unsteadiness, this will be explored later. All angles of attack in the pre-stall regime appear to show a quasi-static region, beyond which $\Delta C_l$ begins to deviate from the static performance.

For post-stall angles, $\alpha_0 = 11, 13, 15^o$, the inflection with amplitude becomes stronger with distinct minima present between $k = 0.20$ and 0.40. The magnitude of lift reduction in this region increases with $\alpha_0$. At $\alpha_0 = 15^o$ the mini-tab is capable of suppressing lift by up to $\Delta C_l = -1.5$. Similar to the pre-stall $\alpha_0$, $\Delta C_l$ exhibits minor variations with $k$ at $A/c = 0.05$ and shows greater sensitivity to $k$ as the amplitude is increased. It is interesting to note the absence of quasi-static behaviour for the post-stall cases and deviations from the static performance occurring at very low reduced frequencies. Once again the influence of the mini-tab deteriorates at high reduced frequencies and amplitudes resulting in a convergence towards $\Delta C_l = 0$.

The performance of the mini-tab with respect to the pitching moment, $\Delta C_m$, is shown in Figure 6. For the pre-stall angles, $\alpha_0 = 0, 3, 5, 7, 9^o$, the response remains somewhat quasi-static at low reduced frequencies. In this regime $\Delta C_m$ lies primarily within the detrimental region for all pre-stall $\alpha_0$. As $k$ is increased, distinct maxima can be seen for the higher amplitudes at

reduced frequencies comparable to those of $\Delta C_l$, which suggests the same mechanism is responsible. The same amplitude effects are also present, where $\Delta C_m$ displays greater sensitivity to $k$ as $A/c$ is increased. At $\alpha_0 = 9^o$ the response shows an inversion which becomes more distinct with increasing $\alpha_0$. Post-stall $\alpha_0$ displays the same minima as $\Delta C_l$ at higher amplitudes, but also show a distinct maxima at higher $k$ of almost equal magnitude between $k = 0.63$ and 0.71. The trends then appear to tend towards $\Delta C_m = 0$ at comparatively higher reduced frequencies.

Figure 5 and Figure 6 show several distinct regimes of behaviour. To understand the cause an extensive PIV campaign was conducted. For the sake of brevity only representative cases will be shown in this article.

## C. Unsteady Flow Fields

The presentation is based on four distinct flow field types: (i) type A: the baseline flow shows *no* coherent LEV formation and the control case displays *no* significant roll-up; (ii) type B: the baseline flow exhibits coherent LEV formation, whereas the control flow shows *no* significant roll-up; (iii) type C: the baseline flow has *no* coherent LEV formation, whilst the control flow contains coherent LEV formation; (iv) type D: the baseline *and* control flows show coherent LEV formation. The following figures will present PIV measurements that illustrate these flow types and the corresponding locations of the cases are marked in Figure 5 and Figure 6 with the label 'A', 'B', 'C' or 'D'.

### *Type A*

Figure 7 presents the phase-averaged lift (Figure 7a) and pitching moment (Figure 7b) along with streamlines overlaid onto normalized velocity magnitude (Figure 7c) at selected phases in the motion for $\alpha_0 = 9^o$, $A/c = 0.05$, $k = 0.94$. This is a representative case for the type A flow field where no coherent vortex shedding or roll-up is seen for the baseline and control airfoils. The added-mass component of the lift and pitching moment is also plotted in Figure 7a and Figure 7b. This is calculated based on the expressions derived by Theordorsen [26] and uses the acceleration measured during the experiments. This provides a reliable estimate of the added-mass force even in highly separated, vortical flows [27]. For this case the maximum lift and moment changes $\Delta C_l$ and $\Delta C_m$ remain close to the static case, and are highlighted with the label 'A' in Figure 5 and Figure 6. The flow fields in Figure 7c show that the baseline flow remains attached or weakly separated throughout the period. The control case, however shows the mini-tab enforcing separation across the chord throughout. Minor velocity variations can

be seen towards the trailing-edge between $t/T = 0.375$ and $0.750$, which appears to be due to weak flapping of the shear layer. For both airfoils the lift variation is virtually sinusoidal with small amplitude and is primarily comprised of the circulatory component. This is consistent with previous observations [6]. A constant offset can be observed between the baseline and control cases, which is close to the difference for the stationary airfoils. The pitching moment on the other hand is solely governed by the added-mass component for attached flows [26] and as such, the baseline case closely agrees well with this estimation whilst the control case deviates somewhat due to flow separation, particularly between $t/T = 0.125$ and $t/T = 0.500$ where the weak flapping of the shear layer can be seen. Despite the weak unsteadiness on the control airfoil, this case leads to no significant change in $\Delta C_l$ and $\Delta C_m$ compared with the static performance.

### *Type B*

Figure 8 presents the phase-averaged lift (Figure 8a) and pitching moment (Figure 8b) along with plots of normalized spanwise vorticity (Figure 8c) at selected phases in the motion period for $\alpha_0 = 15^\circ$, $A/c = 0.50$, $k = 0.24$. This is a representative case for the type B flow field, in which the baseline airfoil exhibits coherent vortex shedding and flow reattachment, whereas the control case shows no significant roll-up. For this case $\Delta C_l$ and $\Delta C_m$ show a drastic reduction as highlighted by the label 'B' in Figure 5 and Figure 6. At $t/T = 0.00$ the baseline airfoil begins the period with fully attached flow. As the period progresses and the plunge velocity, hence $\alpha_{pl}$, increases, the vorticity begins to roll-up aft of the quarter-chord ($t/T = 0.125$) and has grown into a coherent LEV by $t/T = 0.250$. At this point the LEV is approaching the trailing-edge and produces the peak lift and the distinct nose-down pitching moment spike. Note that the added-mass contribution to both $C_l$ and $C_m$ for this low frequency case is virtually negligible. At $t/T = 0.375$ the LEV has been shed from the trailing-edge into the wake, inducing a trailing-edge vortex (TEV). The lift response displays a secondary peak around $t/T = 0.400$. This may be due to the shedding of a secondary, less coherent vortical structure which is well documented in dynamic stall literature [28, 29]; however this is not as clear in the vorticity plots in Figure 8c. From $t/T = 0.500$ to $0.875$ the flow begins to progressively reattach from the leading-edge as the induced angle of attack $\alpha_{pl}$ due to plunging decreases. In stark contrast, the control airfoil exhibits a separated leading-edge shear layer throughout the cycle and subsequently suppressed lift and pitching moment. The difference between the two airfoils is emphasised in Figure 8c at $t/T = 0.250$ in the insets of the streamline plots, where the control case shows no sign of shear layer roll-up.

*Type C*

Figure 9 presents the phase-averaged lift (Figure 9a) and pitching moment (Figure 9b) along with streamline and normalized velocity magnitude plots (Figure 9c) for $\alpha_0 = 3^o$, $A/c = 0.50$, $k = 0.40$. This is a representative case for the type C flow field in which the baseline flow shows no separation, whereas the control flow shows coherent vortex formation. For this case $\Delta C_l$ and $\Delta C_m$ display a distinct maxima in the detrimental region and is highlighted with the label 'C' in Figure 5 and Figure 6. For the baseline airfoil, the flow is attached throughout the cycle. The lift response is almost sinusoidal and the pitching moment agrees well with the added-mass estimation. For the control airfoil, the shear layer emanating from the mini-tab reattaches just downstream around $x/c = 0.5$ at $t/T = 0.00$, forming a closed area of recirculation behind the mini-tab. As the airfoil plunges downwards and $\alpha_{pl}$ increases, the area of recirculation begins to grow as the vorticity accumulates. At $t/T = 0.250$ the flow displays a noticeable increase in velocity magnitude above the mini-tab shear layer. The corresponding vorticity plot in the inset shows shear layer roll-up around the mid-chord position into a coherent vortical structure. This is responsible for the increased lift peak in Figure 9a and the nose-down pitching moment peak in Figure 9b (at a slightly later phase). As the vortex is shed into the wake the lift drops below the baseline case and the pitching moment begins to recover towards the added-mass estimate. This case illustrates the detrimental behaviour of forced separation during unsteady motion at low $\alpha_0$, as shear layer reattachment and roll-up can occur downstream of the separation point resulting in lift increase for the control case.

*Type D*

A type D flow field is achieved when both the baseline and control flow display coherent vortex shedding. This flow field type is associated with near zero $\Delta C_l$ but a wide range of $\Delta C_m$, depending on $\alpha_0$ and $k$, which affect the phase at which the LEV is shed and convected as well as the added-mass contribution. Figure 10 shows four selected cases, which are also highlighted in Figure 5 and Figure 6 with the label 'D'. In part (a), the variation of the pitching moment is shown together with the vorticity fields at two selected phases. For this high-reduced frequency case ($k = 0.94$), the pitching moment is dominated by the added-mass contribution. At $t/T = 0.500$ LEVs produce a negative pitching moment, but their contribution is smaller than that of the added-mass, which is maximum at this instant. At $t/T = 0.625$, the moment arm of the LEVs is larger, but their contribution is still smaller than that of the added-mass. Largest absolute moments occur around $t/T = 0$, resulting in near zero $\Delta C_m$. In order to demonstrate a

11

case with stronger LEV contribution, we present part (b) for $\alpha_0 = 15^o$, with the other parameters unchanged. The local minima observed at $t/T = 0.250$ and $0.625$ can be attributed to the LEV. Comparison with part (a) reveals that the LEV strength in this case appears sufficient enough to counteract the large nose-up pitching moment contribution from the added-mass component. As a result, the phase of the maximum of the absolute value of the moment is delayed compared to the case in part (a). The case in part (b) becomes detrimental in terms of pitching moment.

In part (c), we present a type D case for $k = 0.63$, which is a smaller reduced frequency than the previous cases. The local minimum in pitching moment observed at $t/T = 0.250$ for the control case occurs when the added-mass contribution is zero. For the baseline airfoil on the other hand, LEV formation occurs later in the cycle. For both cases, at $t/T = 0.500$, the moment arm is larger, but the added-mass contribution also reaches its maximum. In the final case presented in part (d), the reduced frequency is the smallest ($k = 0.47$). The LEV contribution for both cases becomes more important. The local minimum of the pitching moment at $t/T = 0.250$ for the control case and at $t/T = 0.500$ for the baseline case are well correlated with the vorticity fields at corresponding phases.

## D. Map of Flow Regimes

The flow field types A, B, C, and D in the previous sections were defined qualitatively based on the flow fields. In order to give a quantitative delineation between type A, B, C and D, a modified pitching moment coefficient is proposed:

$$C_{m,mod} = C_m - C_{m,am} - C_{m,\alpha_0} \qquad (4)$$

The modified pitching moment, $C_{m,mod}$, in Equation 4 is defined as the pitching moment response with the estimated added-mass ($C_{m,am}$) and measured static ($C_{m,\alpha_0}$) components removed. This gives a comparable measure of how the pitching moment response is affected by the LEV. When an LEV forms and convects towards the trailing-edge it induces a nose-down pitching moment spike which results in a distinct deviation from the added-mass estimation. The nose-down pitching moment peaks were located using the *SciPy* Python tool box *scipy.signal.find_peaks* [30] using a peak prominence threshold of $C_{m,mod} \leq -0.09$. To better isolate the LEV signature and imporove the accuracy of the search method, only the nose-down (negative) portions of the signal were considered. Using this analysis, the boundary of coherent LEV formation can be estimated for each case tested as a function of $\alpha_0$, $k$ and $A/c$,

giving an approximation of the flow field type boundaries. This algorithm based on the pitching moment peak was tested against all available PIV measurements (total of 30 cases) and confirmed to detect the absence or presence of the LEV formation in the vast majority of the cases.

The resulting boundaries of coherent LEV formation for the baseline airfoil (dashed lines) and control airfoil (solid lines) are shown on the contour plots of the lift change $\Delta C_l$ in Figure 11 as a function of $\alpha_0$ and $k$. Each boundary is plotted as a band due to the discrete number of reduced frequencies tested. Note that at $A/c = 0.10$ and $0.20$ the boundary lines terminate where no $C_{m,mod}$ peak was detected, indicating that coherent LEV formation occurs beyond the maximum $k$ tested. The areas of flow field type are indicated with the labels A, B, C and D. Additionally the PIV test (validation) cases are also shown as symbols and are grouped based on qualitative assessment of the flow field type. Consider first the amplitude extreme of $A/c = 0.05$. Based on the PIV measurements, almost all combinations of $\alpha_0$ and $k$ produce the type A flow field, where the plunging velocity is insufficient to produce roll-up on either airfoil. The exception is for $\alpha_0 = 15^0$ at $k = 0.94$ where the flow field assessment indicates a type B flow field. The algorithm based on the pitching moment predicts type A for all cases. It is seen that type A produces a decrease in $\Delta C_l$, except at small incidences $\alpha_0 \leq 3^0$. The mini-tab induces flow separation on the upper surface at $\alpha_0 = 0^0$ and small incidences, and the resulting negative pressure causes an increase in the lift force compared to the baseline case. The change in lift is similar to the static data with minimal effect of $k$, and hence follows the quasi-steady trend.

At the other extreme $A/c = 0.50$ the parameter space consists of all flow field types (A, B, C and D) and available PIV cases agree well with the algorithm based on the pitching moment. Again, the type A flow field occurs for all pre-stall $\alpha_0$ as $k$ approaches zero. This quickly transitions to a type C for low $\alpha_0$ as $k$ is increased. Type B transitions to type D flow field for high $\alpha_0$ as $k$ is increased. Type D causes slightly beneficial or slightly detrimental effects on the maximum lift force. Also presented in Figure 11 is the intermediate amplitudes $A/c$ which illustrate how the type A, B, C and D flow fields develop. It is clear that type B is always beneficial, type A is mostly beneficial (except at small $\alpha_0$), type C is mostly detrimental, and type D is mixed.

Equivalent contour plots for $\Delta C_m$ are presented in Figure 12. For $A/c = 0.05$, type A mostly causes an increased pitching moment, following the same trend as the stationary case. For $A/c = 0.50$ the boundary of $\Delta C_m = 0$ encapsulating the type B flow field is well defined and is in agreement with the LEV formation boundaries. The development of this region can be seen as the amplitude is increased from $A/c = 0.05$ to $0.5$. Type B causes a decrease in the pitching

moment, type A is mostly detrimental and type D is mixed. We note that type C is particularly detrimental at low incidences. Type B is beneficial for both lift and pitching moment, and is observed at post-stall incidences at lower reduced frequencies ($k < 0.3$), which are comparable to gust frequencies on civil aircraft as well as rotorcraft applications.

For fixed-wing applications, control of lift (hence, bending moment) is more important than the control of pitching moment. It is clear that the desired flow field types for lift control is type A and B, for which reattachment on the upper surface is prevented with the use of mini-tab. In Figure 11 the indicator for this desired behaviour is where $\Delta C_l < 0$. Figure 13 shows the contours of $\Delta C_l = 0$ for all $A/c$ as a function of $\alpha_0$ and different variables. Figure 13a displays the contours of $\Delta C_l = 0$ as a function of $k$, which shows no collapse with $k$. The gradient dependence on $A/c$ at low $k$ suggests that scaling with $St_A = fA/U_\infty$ may be more appropriate as shown in Figure 13b. A reasonable amount of collapse can be seen at low $St_A$ for pre-stall incidences, where the boundary between beneficial and detrimental performance increases almost linearly with $\alpha_0$. Figure 13c presents the boundaries in terms of the maximum induced angle of attack:

$$\alpha_{pl,max} = tan^{-1}\frac{\pi f A}{U_\infty} = tan^{-1}(\pi St_A) \tag{5}$$

attained during the motion. Interestingly the performance boundary lines up well with the line of $\alpha_0 = \alpha_{pl,max}$, implying that the switch to detrimental performance occurs when the total effective angle of attack reduces to zero during the motion:

$$\alpha_{eff,min} = \alpha_0 - tan^{-1}(\pi St_A) = 0 \tag{6}$$

Although this is a simplified interpretation, it appears to hold in this case. For $\alpha_{pl,max} > \alpha_0$, the minimum effective angle of attack becomes negative, and the contours of $\Delta C_l = 0$ then begin to deviate from the straight line.

An interesting feature in Figure 5 is the maxima and minima of $\Delta C_l$ displayed in the pre- and post-stall regimes respectively. These regions of extrema lie in the regions of B and C in Figure 11. We present the approximate locations of these peaks in terms of $k$ and $St_A$ in Figure 14. A reasonable degree of collapse can be observed in Figure 14a with respect to $k$. The maxima for all $A/c$ occur across a particular frequency band of $k = 0.35$ to $0.60$; the large outliers for $A/c = 0.2$ and $0.3$ are most likely due to a lack of resolution in $k$ when extracting

the maxima. A monotonic increase is present for the post-stall minima occurrences, increasing from $k = 0.2$ to $0.5$ as $\alpha_0$ is increased. In contrast, no distinct scaling can be seen with $St_A$ in Figure 14b. Hence, whereas the borderline between the beneficial and detrimental regions is better correlated with $St_A$ (Figure 13), we find the locations of the extrema scale better with the reduced frequency (Figure 14).

### E. Transient Response

The study has so far considered the mini-tab's performance under periodic conditions, however it is also essential to consider the transient response to such disturbances, analogous to a discrete gust or extreme manoeuvre. Further experiments were conducted to examine the response to impulsively started plunging oscillations. Figure 15 presents these data for selected reduced frequencies at $\alpha_0 = 15°$ and $A/c = 0.5$. The motion starts at $t/T = 0$ in these plots.

Consider first the time history of the lift coefficient at $k = 0.24$ in Figure 15. A striking difference with the response of the baseline airfoil can be seen between the first and second motion cycles. The peak lift increases by around 100% from $t/T = 0.25$ to $t/T = 1.25$ which then holds for subsequent cycles. In contrast, the control airfoil response displays no significant cycle to cycle variation. This is also reflected in the pitching moment responses, where a large nose-down pitching moment spike emerges at the same phase, $t/T = 1.25$, indicating a distinct change in vortex formation and shedding. This is typical of a type B flow field. As $k$ is increased, the lift amplitude as well as the mean lift increase significantly for both the baseline and control airfoils. At $k = 0.94$ the lift response takes multiple cycles to reach an asymptote, which suggests that periodic conditions are achieved at a critical convective time rather than cycle number. Similar dependence on convective time is present in the pitching moment responses.

The parameters $\Delta C_l$ and $\Delta C_m$ were extracted in each cycle to determine the mini-tab's performance for impulsively started plunging oscillations. Figure 16 presents this data for $\alpha_0 = 5$, $9$ and $15°$ at $A/c = 0.5$. The first four cycles are compared against the periodic response shown in black. Interestingly, the mini-tab performance shows relatively little variation with $k$ during the first cycle, with the exception of $\Delta C_m$ for $\alpha_0 = 9°$. For all $\alpha_0$ tested, we observe mostly beneficial performance ($\Delta C_l < 0$ and $\Delta C_m < 0$), except for $\Delta C_m$ at $\alpha_0 = 5°$. Compared to the periodic counterpart, there is an improvement in most cases as well, which is a promising result for performance during discrete gust encounters. In particular, for fixed-wing applications, $\Delta C_l$ is always negative (therefore, beneficial) for the first cycle. At low values of $k$ the mini-tab

performance agrees well with the periodic performance after the first cycle. At high values of $k$ more cycles are required to approach the periodic response.

To show the cause of this transient behavior, Figure 17 presents the flow field measurements for $\alpha_0 = 15^{\circ}$ at $A/c = 0.5$ and $k = 0.24$. Lift and pitching moment are shown in Figure 17a and Figure 17b respectively for reference. Peak lift and nose-down pitching moment in the first cycle is achieved around $t/T = 0.25$ for both airfoils. The baseline airfoil and control airfoil display largely separated flow at this instant. During the upstroke, the effective angle of attack is below the mean angle of attack, resulting in a reattaching flow over the baseline airfoil and increased lift at $t/T = 1.0$. In contrast, the control airfoil maintains a separated shear layer. This has significant consequences for the subsequent cycle. A coherent LEV is present over the baseline airfoil at $t/T = 1.25$ (see the inset), in stark contrast to the same phase of the previous cycle ($t/T = 0.25$). Flow reattachment prior to LEV formation is a significant factor that influences the strength and the location of the shear layer and its subsequent roll-up. In contrast, the control airfoil at $t/T = 1.25$ matches that of $t/T = 0.25$ and is highlighted by the similarity in the lift and moment, see Figure 17a and Figure 17b. The fixed separation point, which is further away from the airfoil surface does not allow roll-up of vorticity at any instant.

## IV. Conclusions

A novel approach to reduce the peak lift and pitching moment on a plunging airfoil was investigated through force, moment, and velocity measurements. A passively deployed mini-tab (flow fence) device was tested to determine the efficacy of forced flow separation near the leading-edge of a NACA 0012 airfoil to alleviate high loads during extreme unsteady events, particularly where organized vortical structures can form. Although this device can cause drag increase for short durations during a gust encounter or unsteady manoeuvre, potential lift and moment alleviation is more important in designing a lighter aircraft, hence achieving drag reduction. The performance of the device was compared to a clean "baseline" NACA0012 airfoil and was determined through unsteady lift, pitching moment and flow field measurements. In static conditions the mini-tab enforces flow separation across the chord, leading to a free-shear layer. During dynamic plunging oscillations, the mini-tab's performance depended drastically on the behaviour of the free-shear layer, which varies greatly with the geometric angle of attack, amplitude and reduced frequency of the plunging motion. The mini-tab produces four types of flow regimes, depending on the shear layer behaviour. For type A, neither the baseline flow nor the control case displays shear layer roll-up. In type B, the baseline flow exhibits coherent LEV formation, whereas the control flow shows no significant

roll-up. For type C, the baseline flow has no coherent LEV formation, whilst the control flow contains coherent LEV formation. In type D, both the baseline and control airfoils show coherent LEV formation.

Type A and B are associated with beneficial lift control behaviour and occur at low plunge velocities and low $k$. Significant lift and moment decreases were observed at post-stall angles of attack and low reduced ftrequencies (type B). For this type, the mini-tab delays or prevents the roll-up of vorticity over the airfoil. At low angles of attack, shear layer reattachment behind the mini-tab is the primary cause of the performance degradation and precedes coherent shear layer roll-up (type C); this critical point was found to scale with $St_A$ and occur when the induced angle of attack during motion was approximately equal to the geometric angle of attack, i.e. the total effective angle of attack reaches zero. Type B and C flow fields show distinct maxima/minima at particular frequencies that scale primarily with the reduced frequency for all amplitudes tested. Finally, the transient response to impulsively started plunging oscillations revealed the importance of wake development on the mini-tab performance. Across the majority of the tests, the performance was significantly more beneficial during the first motion cycle, which is highly beneficial for a device operating in a more realistic gust or manoeuvre scenario.

## References

[1] McCroskey, W. J., "Unsteady Airfoils," *Annual Review of Fluid Mechanics,* Vol. 14, January, 1982, pp. 285-311.
https://doi.org/10.1146/annurev.fl.14.010182.001441

[2] Ekaterinaris, J., and Platzer, M., "Computational Prediction of Airfoil Dynamic Stall," *Progress in Aerospace Sciences*, Vol. 33, Nos. 11-12, 1998, pp. 759–846.
https://doi.org/10.1016/S0376-0421(97)00012-2

[3] Corke, T. C., and Thomas, F. O., "Dynamic Stall in Pitching Airfoils: Aerodynamic Damping and Compressibility Effects," *Annual Review of Fluid Mechanics*,. Vol. 47, January, 2015, pp. 479-505.
https://doi.org/10.1146/annurev-fluid-010814-013632

[4] Benton, S., and Visbal, M., "The Onset of Dynamic Stall at a High, Transitional Reynolds Number," *Journal of Fluid Mechanics*, Vol. 861, February, 2019, pp. 860-885.
https://doi.org/10.1017/jfm.2018.939

[5] Cleaver, D. J., Wang, Z., Gursul, I., and Visbal, M. R., "Lift Enhancement by Means of Small-Amplitude Airfoil," *AIAA Journal*, Vol. 49, No. 9, 2011, pp. 2018-2033.
http://dx.doi.org/10.2514/1.J051014

[6] Chieregin, N., Cleaver, D., and Gursul, I., "Unsteady Lift and Moment of a Periodically Plunging Airfoil," *AIAA Journal*, Vol. 57, No. 1, 2019, pp. 208-222.
https://doi.org/10.2514/1.J057634

[7] Gursul, I., and Ho, C. M., "High Aerodynamic Loads on an Airfoil Submerged in an Unsteady Stream," *AIAA Journal*, Vol. 30, No. 4, 1992, pp. 1117-1119.
https://doi.org/10.2514/3.11034

[8] Gursul, I., Lin, H., and Ho, C. M., "Effects of Time Scales on Lift of Airfoils in an Unsteady Stream," *AIAA Journal*, Vol. 32, No. 4, 1994, pp. 797-801.
https://doi.org/10.2514/3.12055

[9] Choi, J., Colonius, T., and Williams, D. R., "Surging and Plunging Oscillations of an Airfoil at Low Reynolds Number," *Journal of Fluid Mechanics*, Vol. 763, January, 2014, pp. 237-253.
https://doi.org/10.1017/jfm.2014.674

[10] Greenblatt, D., and Wygnanski, I., "Dynamic Stall Control by Periodic Excitation, Part 1: NACA0015 Parametric Study," *Journal of Aircraft*, Vol. 38, No. 3, 2001, pp. 430-438.
https://doi.org/10.2514/2.2810

[11] Ekaterinaris, J. A., "Numerical Investigations of Dynamic Stall Active Control for Incompressible and Compressible Flows," *Journal of Aircraft*, Vol. 39, No. 1, 2002, pp. 71-78.
https://doi.org/10.2514/2.2897

[12] Karim, M. A., and Acharya, M., "Suppression of Dynamic-Stall Vortices over Pitching Airfoils by Leading-Edge Suction," *AIAA Journal*, Vol. 32, No. 8, 1994, pp. 1647-1655.
https://doi.org/10.2514/3.12155

[13] Post, M. L., and Corke, T. C., "Separation Control Using Plasma Actuators: Dynamic Stall Vortex Control on Oscillating Airfoil," *AIAA Journal*, Vol. 44, No. 3, 2006, pp. 125-135.
https://doi.org/10.2514/1.22716

[14] Chandrasekhara, M. S., Wilder, M. C., and Carr, L. W., "Unsteady Stall Control Using Dynamically Deforming Airfoils," *AIAA Journal*, Vol. 36, No. 10, 1998, pp. 1792-800.
https://doi.org/10.2514/2.294

[15] Freymuth, P., Jackson, S., and Bank, W., "Toward dynamic separation without dynamic stall," *Experiments in Fluids*, Vol. 7, No. 3, 1988, pp. 187-196.
https://doi.org/10.1007/BF02332983

[16] Carr, L. W., Chandrasekhara, M. S., Wilder, M. C., and Noonan, K. W., "Effect of Compressibility on Suppression of Dynamic Stall Using a Slotted Airfoil," *Journal of Aircraft*, Vol. 38, No. 2, 2001, pp. 296-309.
https://doi.org/10.2514/2.2762

[17] Heathcote, D. J., Gursul, I., and Cleaver, D. J., "Aerodynamic Load Alleviation Using Minitabs," *Journal of Aircraft*, Vol. 55, No. 5, 2018, pp. 2068-2077.
https://doi.org/10.2514/1.C034574

[18] Schmitt, N. P., Rehm, W., Pistner, T., Zeller, P., Diehl, H., and Navé, P., "The AWIATOR airborne LIDAR turbulence sensor," *Aerospace Science and Technology*, Vol. 11, Nos. 7-8, 2007, pp. 546–552.
https://doi.org/10.1016/j.ast.2007.03.006

[19] Heathcote, S., "Flexible Flapping Airfoil Propulsion at Low Reynolds Numbers," Ph.D. Thesis, Department of Mechanical Engineering, University of Bath, Bath, England, U.K., 2006.

[20] Cleaver, D. J., Wang, Z., and Gursul, I., "Vortex Mode Bifurcation and Lift Force of a Plunging Airfoil at Low Reynolds Numbers," *48th AIAA Aerospace Sciences Meeting*, Orlando, FL, 2010, pp. 1-16.
https://doi.org/10.2514/6.2010-390

[21] Kim, D. H., Chang, J. W., and Chung, J., "Low-Reynolds-Number Effect on Aerodynamic Characteristics of a NACA 0012 Airfoil," *Journal of Aircraft*, Vol. 48, No. 4, 2011, pp. 1212-1215.
https://doi.org/10.2514/1.C031223

[22] Wang, S., Zhou, Y., Mahbub Alam, Md., and Yang, H., "Turbulent intensity and Reynolds number effects on an airfoil at low Reynolds numbers," *Physcis Of Fluids*, Vol. 26, No. 115107, 2014, pp. 1-25.
https://doi.org/10.1063/1.4901969

[23] Ohtake, T., Nakae, Y., and Motohashi, T., "Nonlinearity of the Aerodynamic Characteristics of NACA 0012 Aerofoil at Low Reynolds Numbers (In Japanese)," *Japan Society for Aeronautical and Space Sciences*, Vol. 55, No. 644, 2007, pp. 439-445.
https://doi.org/10.2322/jjsass.55.439

[24] Schluter, J. U., "Lift Enhancement at Low Reynolds Numbers Using Self-Activated Movable Flaps," *Journal of Aircraft*, Vol. 47, No. 1, 2010, pp. 348-351.
https://doi.org/10.2514/1.46425

[25] Heathcote, D. J., "Mini-Tabs for Aerodynamic Loads Alleviation," Ph.D. Thesis, University of Bath, Bath, England, U.K., 2017.

[26] Theodorsen, T., "General Theory of Aerodynamic Instability and the Mechanics of Flutter", NACA TR-496, January 1949.

[27] Corkery, S., Babinsky, H., Graham, W., "Quantification of added-mass effects using particle image velocimetry for a translating and rotating flat plate," *Journal of Fluid Mechanics*, Vol. 870, July, 2019, pp. 492-518.
https://doi.org/10.1017/jfm.2019.231

[28] McCroskey, W., "The Phenomenon of Dynamic Stall," NASA TR-81264, March 1981.

[29] Mulleners, K., and Raffel, M., "The onset of dynamic stall revisited," *Experiments in Fluids*, Vol. 52, No. 3, 2012, pp. 779-793.
https://doi.org/10.1007/s00348-011-1118-y

[30] The Scipy Community 2019, *scipy.signal.find_peaks*, viewed September 2019,
https://docs.scipy.org/doc/scipy/reference/generated/scipy.signal.find_peaks.html
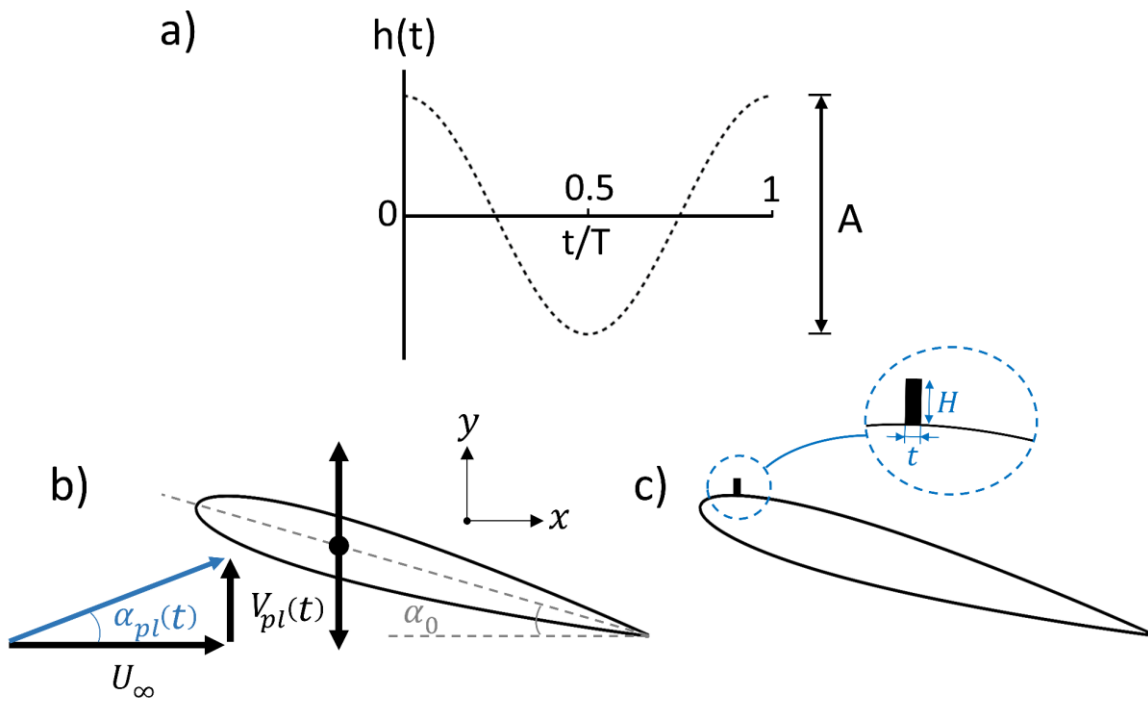
**Figure 1:** a) Airfoil motion profile, b) plunging parameters, c) mini-tab geometry.
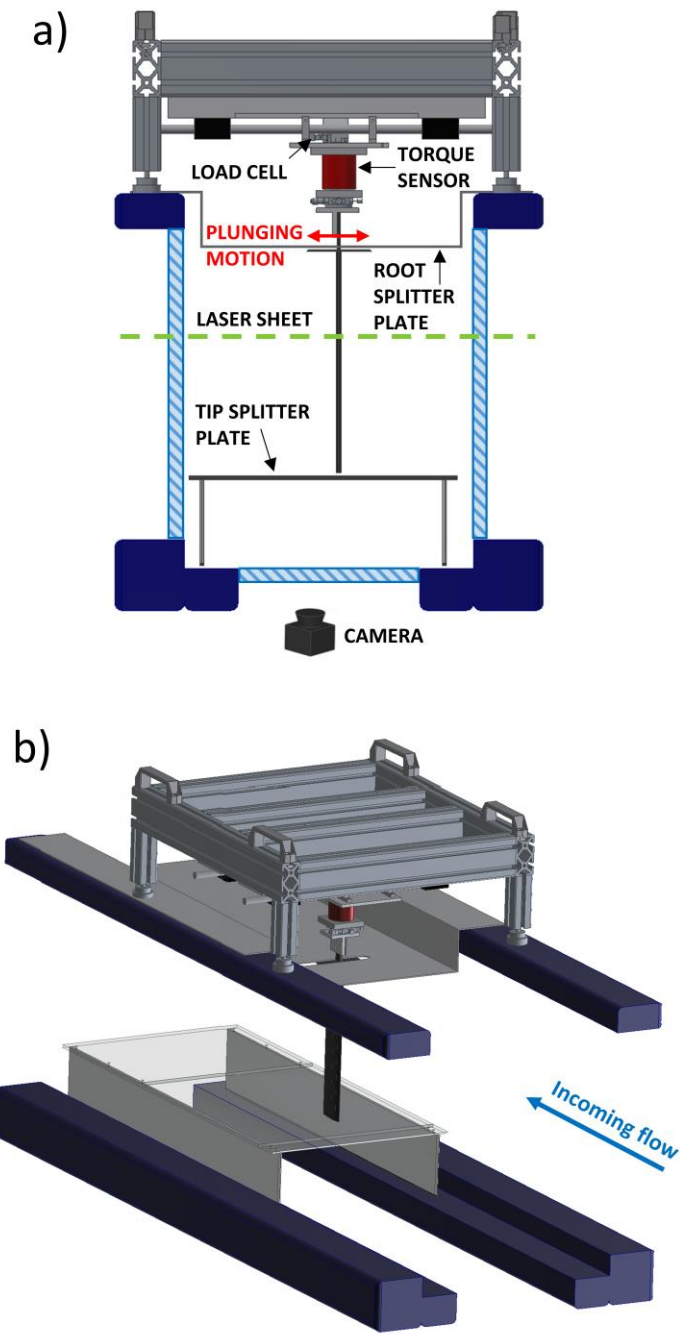
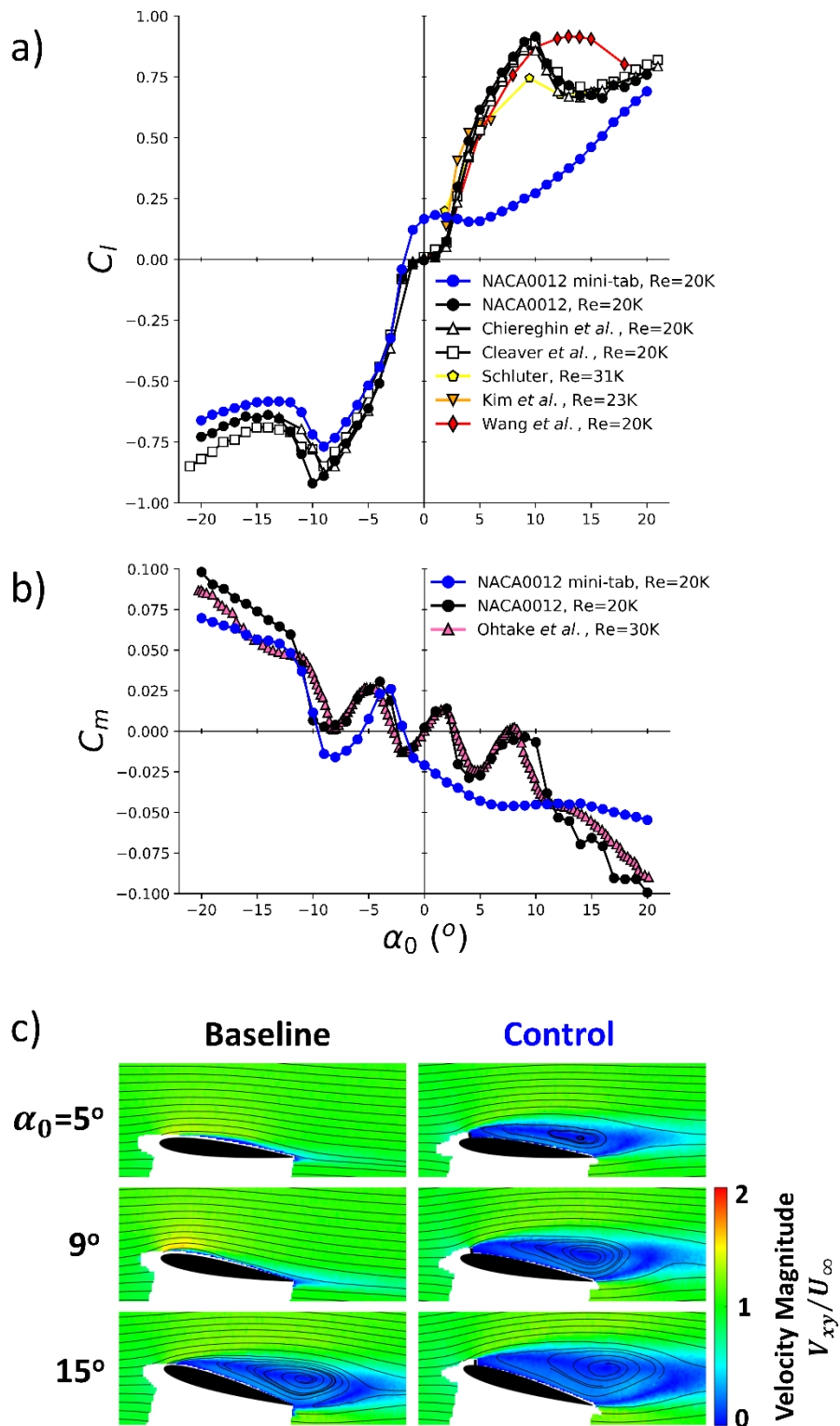**Figure 2:** Water tunnel test rig, a) front view, b) isometric view.

**Figure 3:** a) Static lift coefficient, b) static pitching moment coefficient and c) velocity magnitude plots for selected $\alpha_0$.
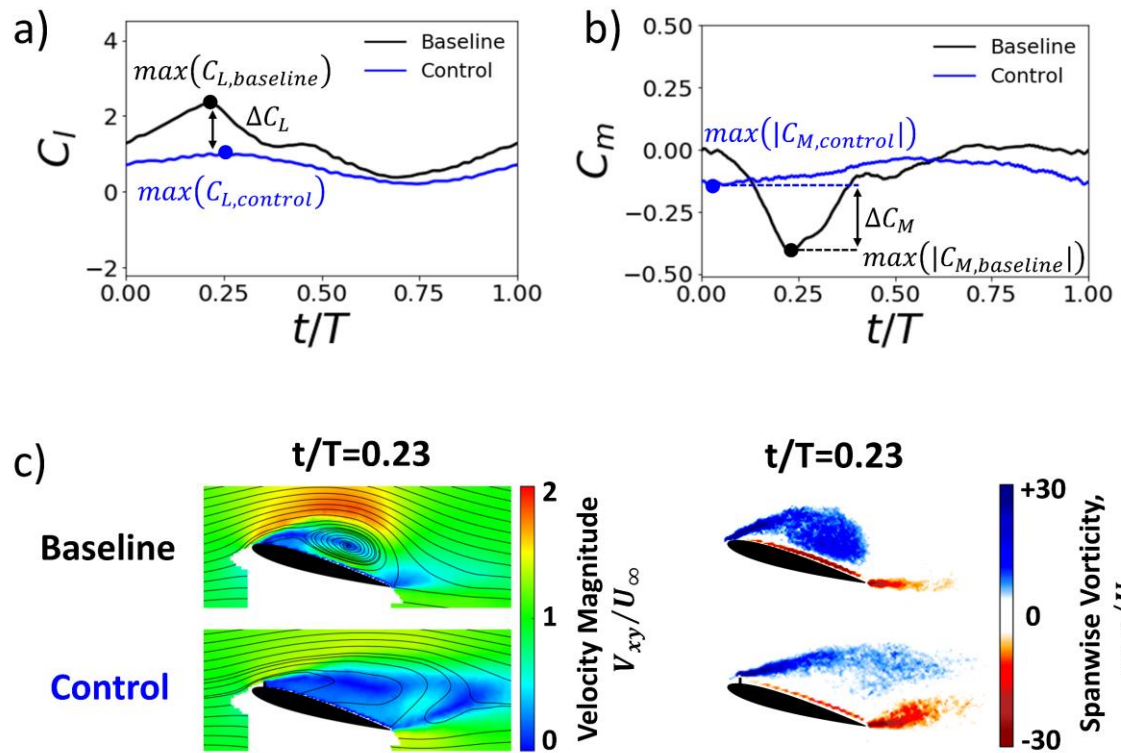
**Figure 4:** Example case: $\alpha_0$=15⁰, *A/c*=0.5, *k*=0.24; a) phase-averaged lift coefficient, b) phase-averaged pitching moment coefficient, c) normalized velocity and vorticity fields.
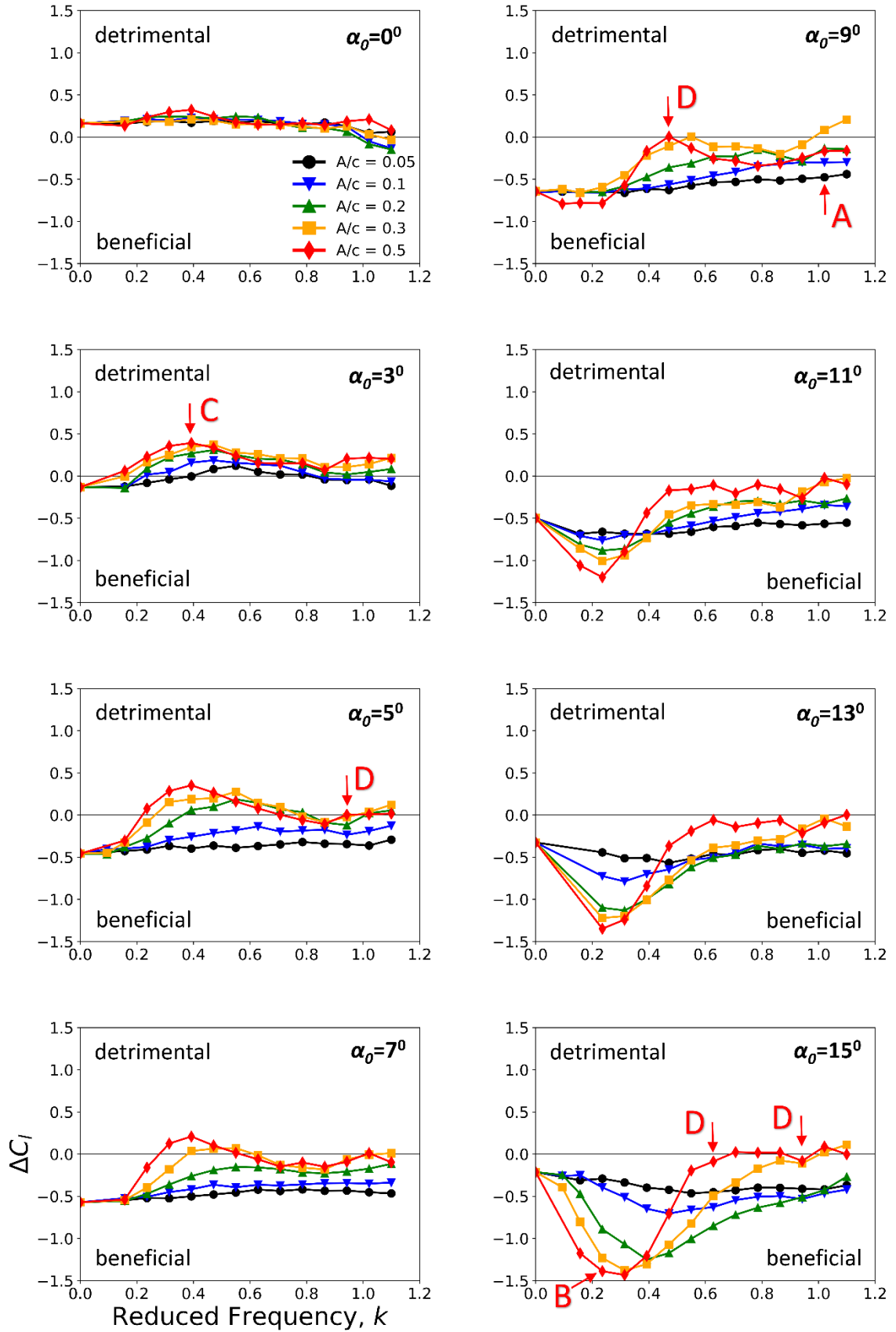
**Figure 5:** Lift performance of mini-tab.
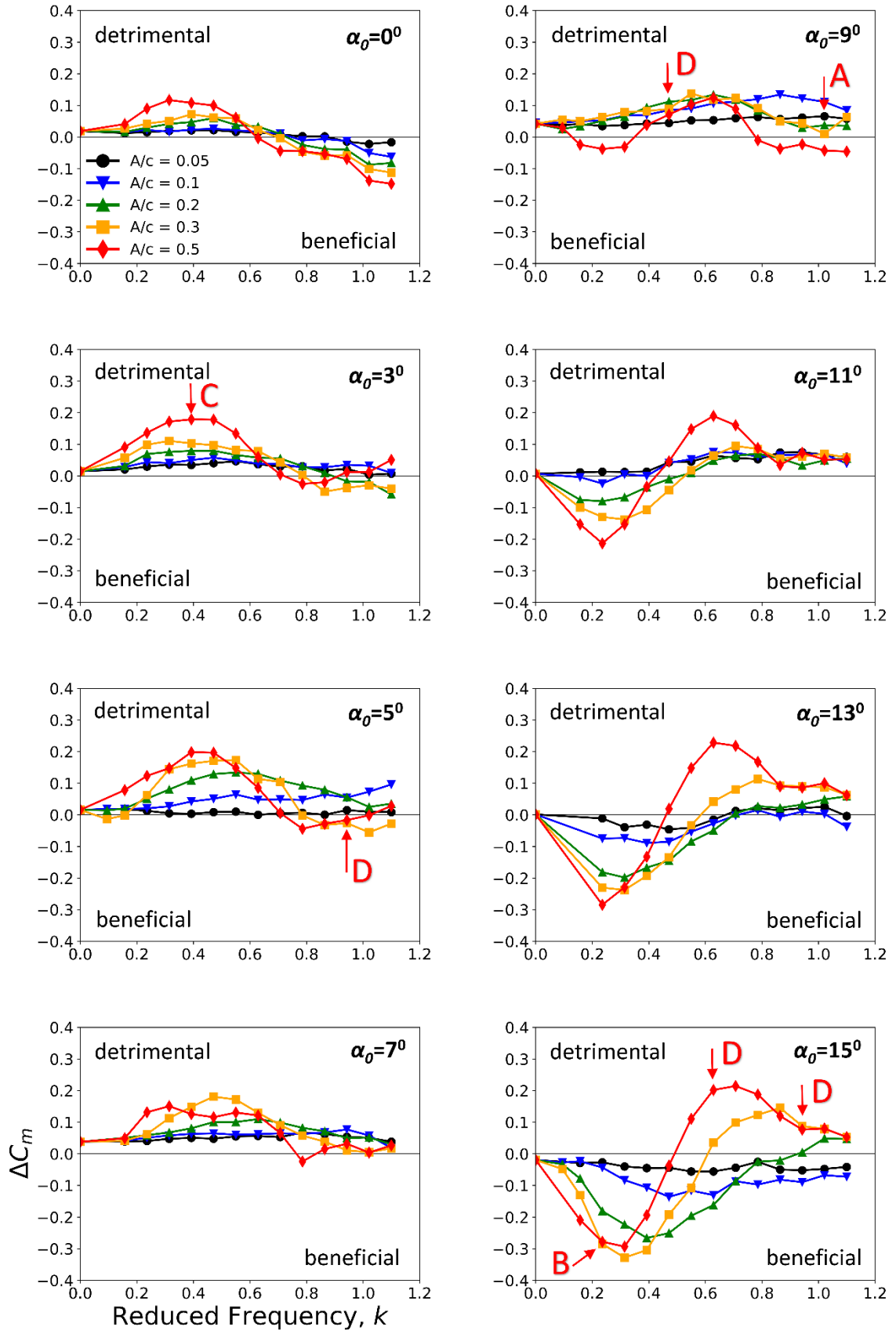
**Figure 6:** Pitching moment performance of mini-tab.
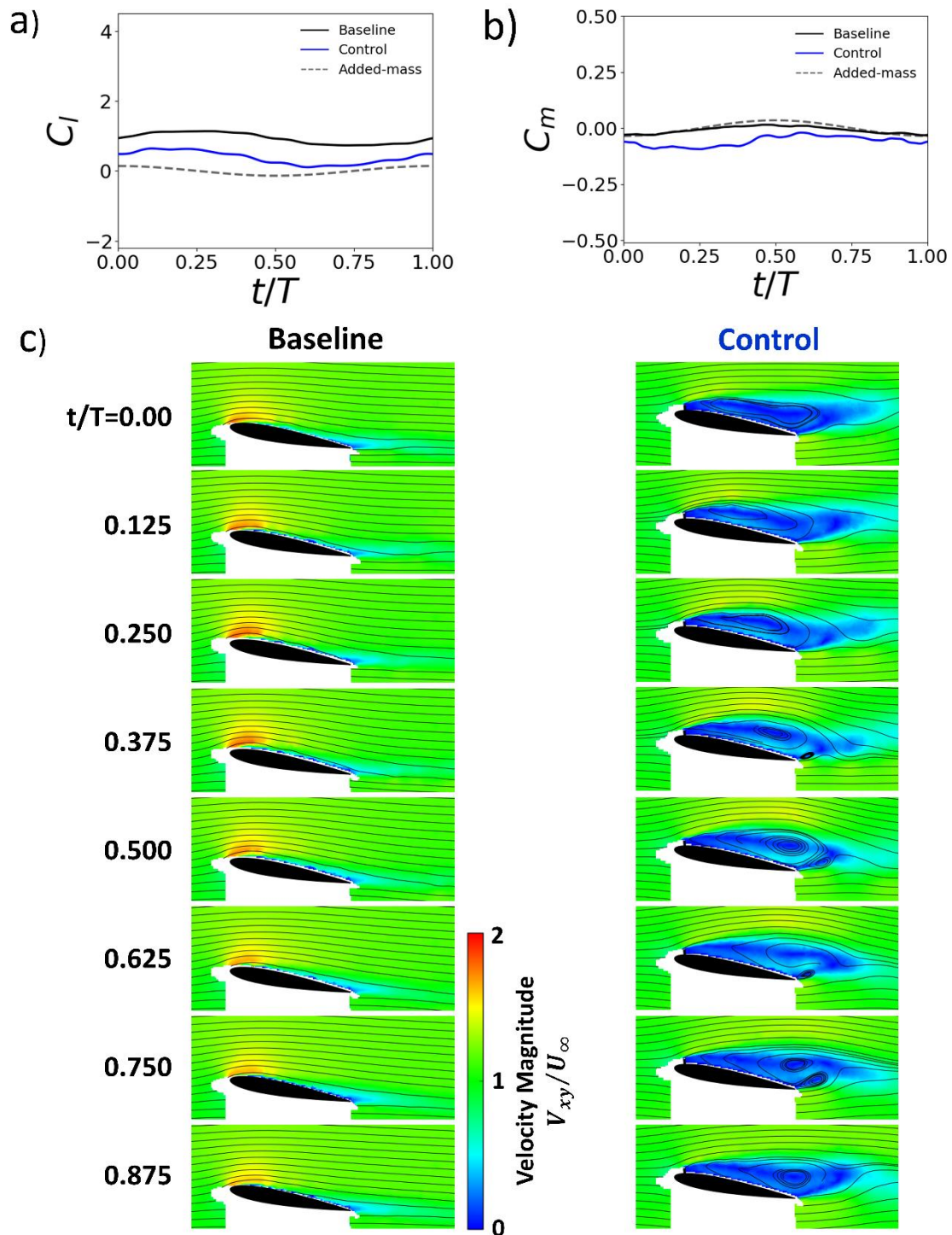
**Figure 7:** Type A flow field - $\alpha_0$=9°, *A/c*=0.05, *k*=0.94: a) phase-averaged lift coefficient, b) phase-averaged pitching moment coefficient, c) normalized velocity magnitude with streamlines.
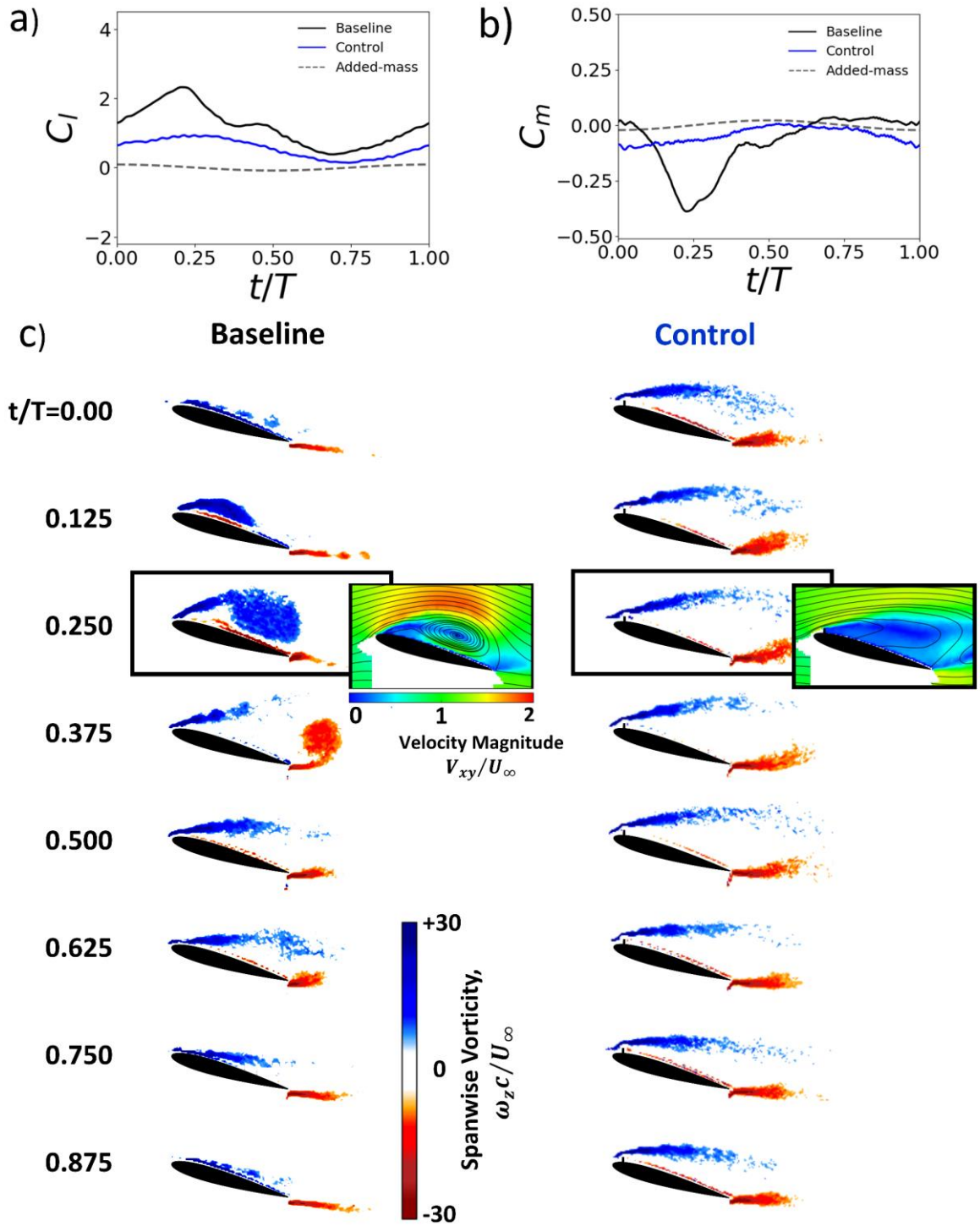
**Figure 8:** Type B flow field - $\alpha_0$=15º, $A/c$=0.5, $k$=0.24: a) phase-averaged lift coefficient, b) phase-averaged pitching moment coefficient, c) normalized spanwise vorticity.
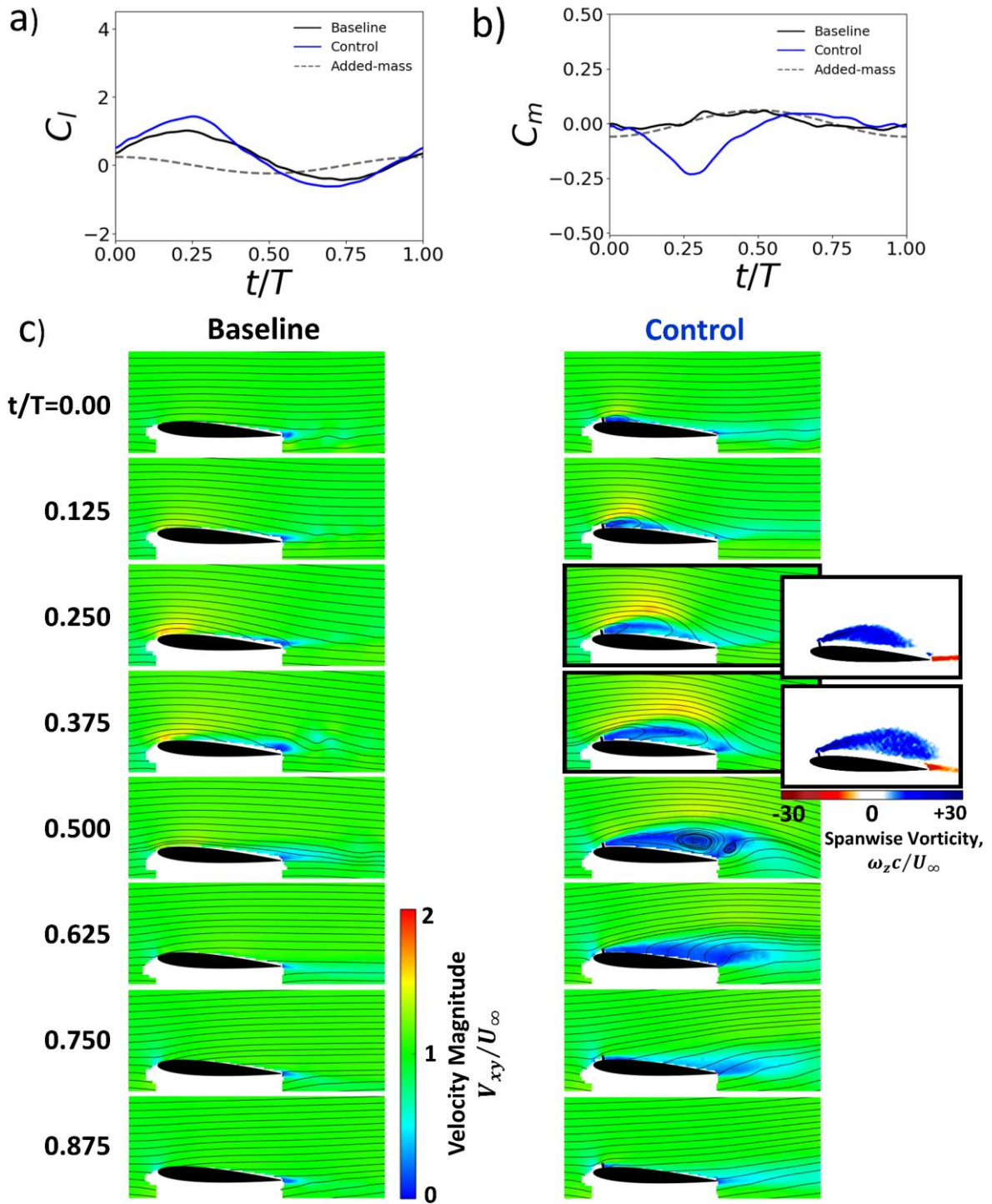
**Figure 9**: Type C flow field - $\alpha_{0}=3^{o}$, $A/c$=0.5, $k$=0.40: a) phase-averaged lift coefficient, b) phase-averaged pitching moment coefficient, c) normalized velocity magnitude with streamlines.
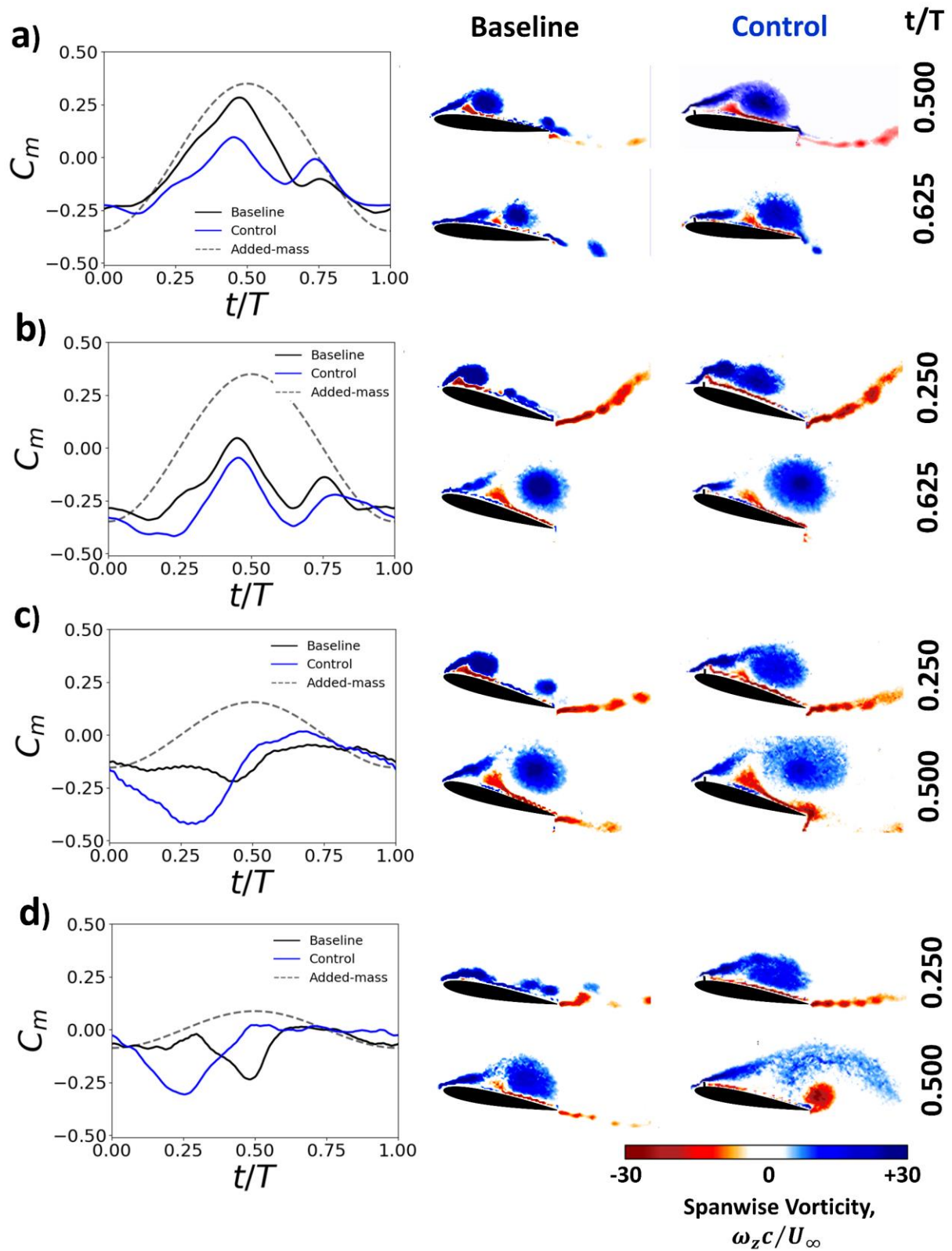
**Figure 10:** Type D flow field – Phase-averaged pitching moment coefficient with normalized spanwise vorticity flow fields at select phases: a) $\alpha_0=5°$, $A/c=0.5$, $k=0.94$, b) $\alpha_0=15°$, $A/c=0.5$, $k=0.94$, c) $\alpha_0=15°$, $A/c=0.5$, $k=0.63$, d) $\alpha_0=9°$, $A/c=0.5$, $k=0.47$.
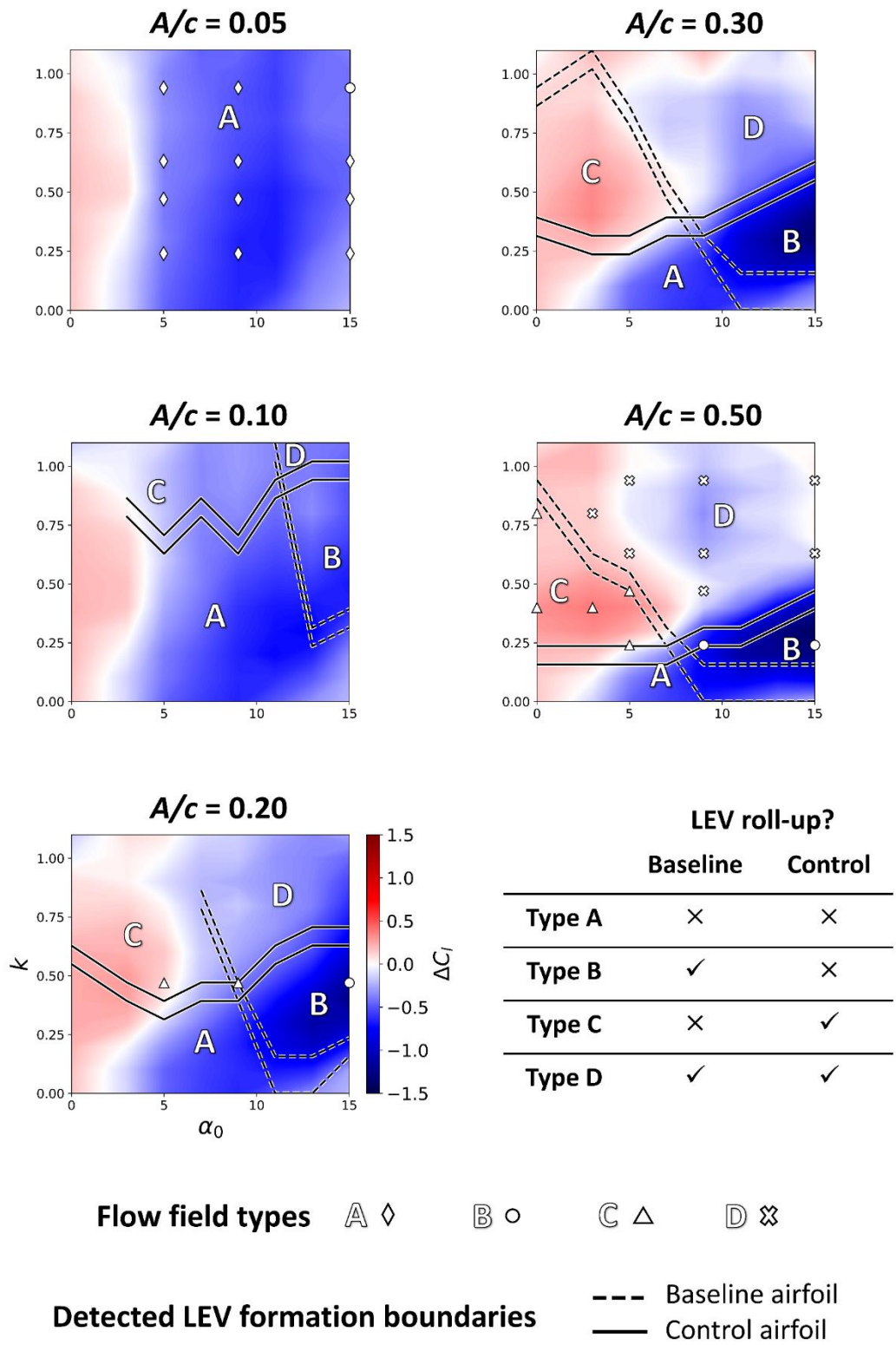
**Figure 11:** Contour plots of mini-tab lift performance with LEV formation boundaries.
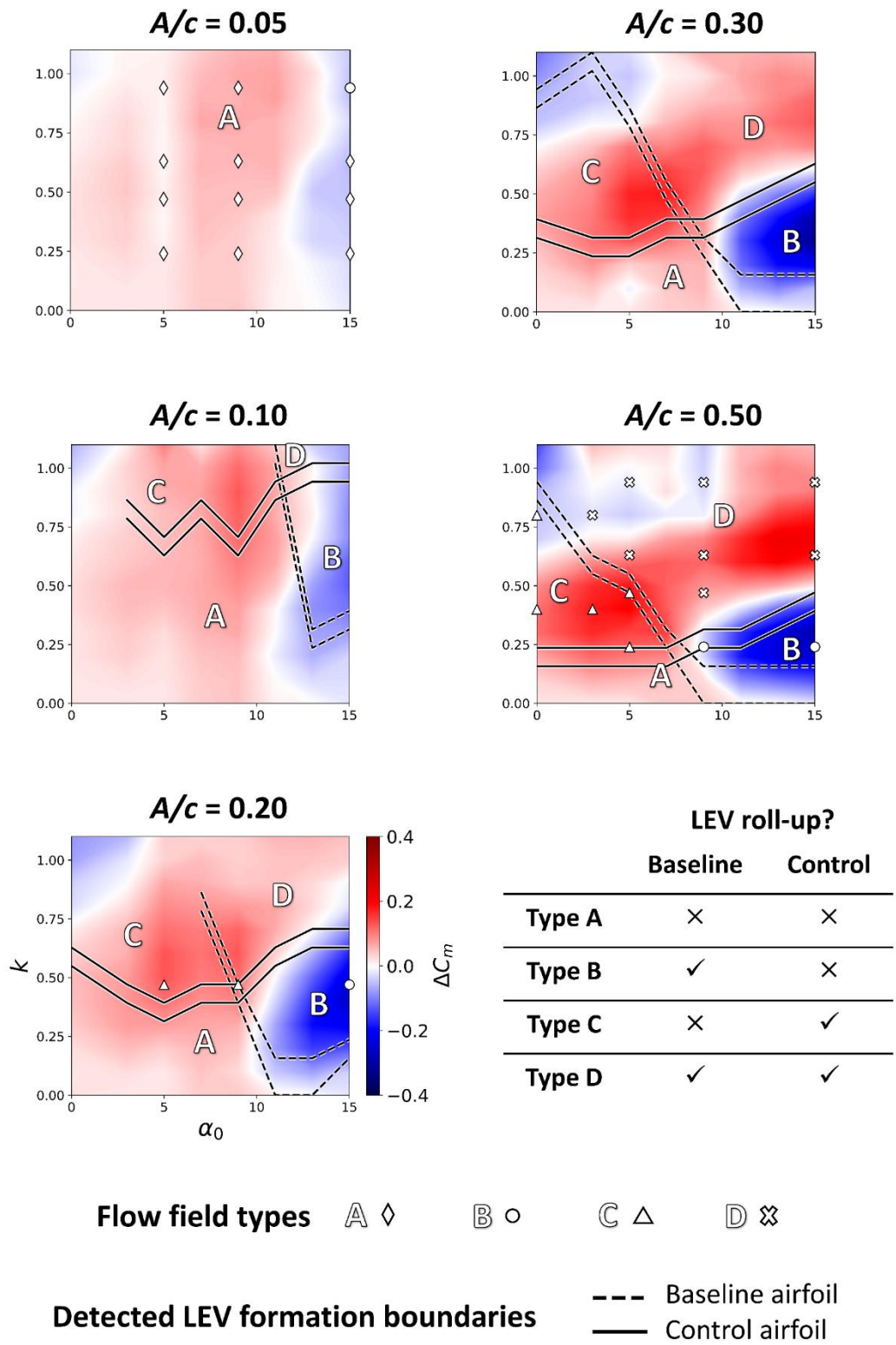
**Figure 12:** Contour plots of mini-tab pitching moment performance with LEV formation boundaries.
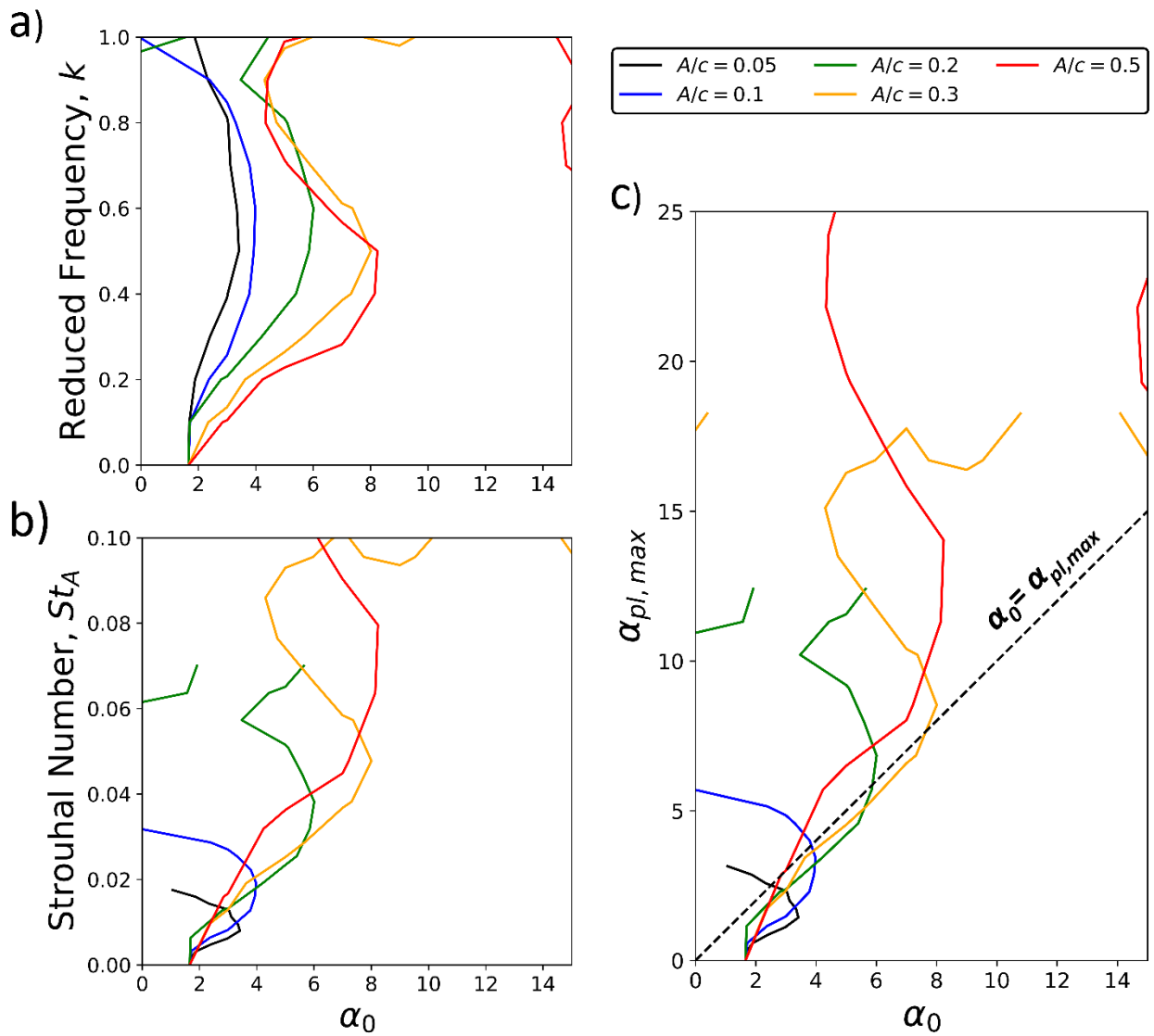
**Figure 13:** Boundary of $\Delta C_l = 0$ as a function of $k$, $St_A$, $\alpha_{pl,max}$ and $\alpha_0$ for different values of A/c.
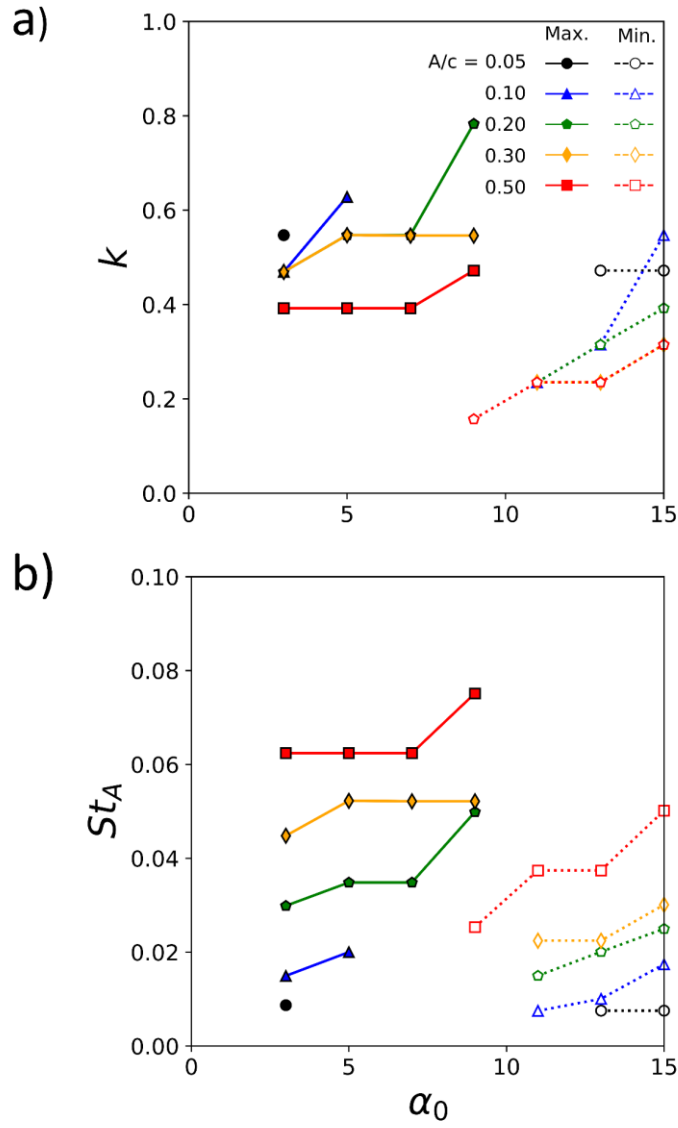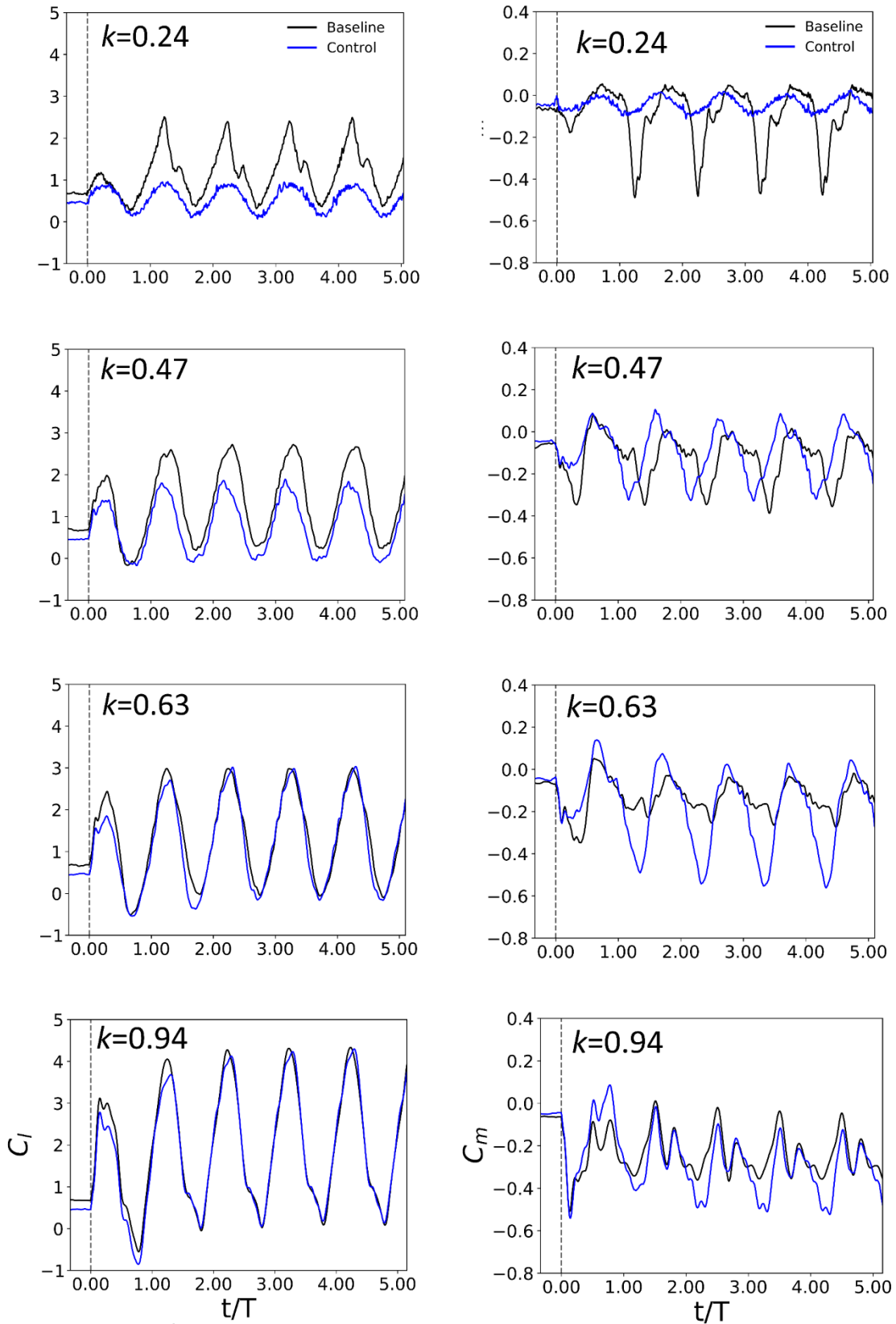
**Figure 14:** Frequencies of the minima/maxima of $\Delta C_l$.

**Figure 15:** Lift (left column) and pitching moment (right column) response for impulsively started plunging oscillations at different $k$; $\alpha_0$=15°, $A/c$=0.5.
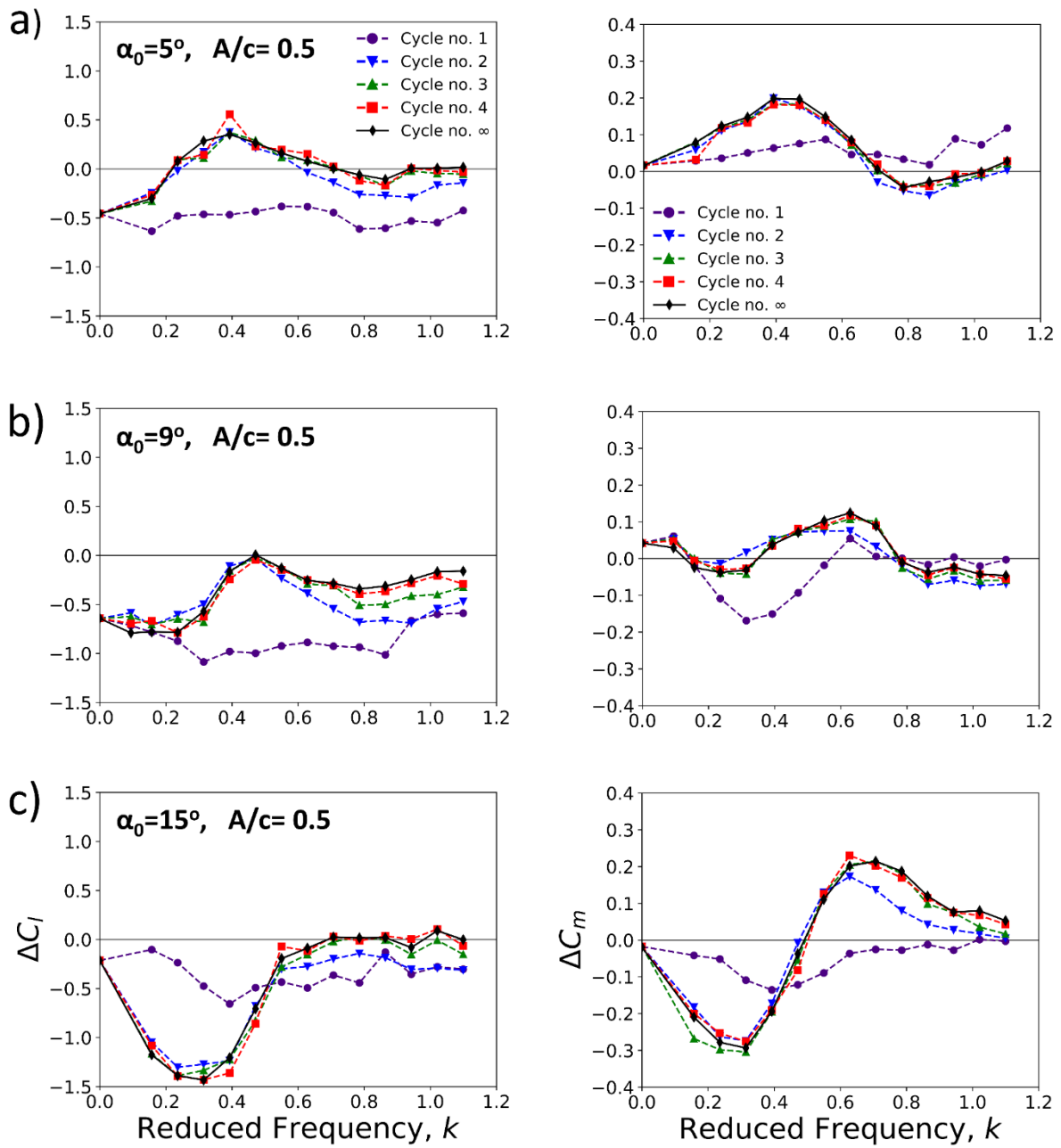
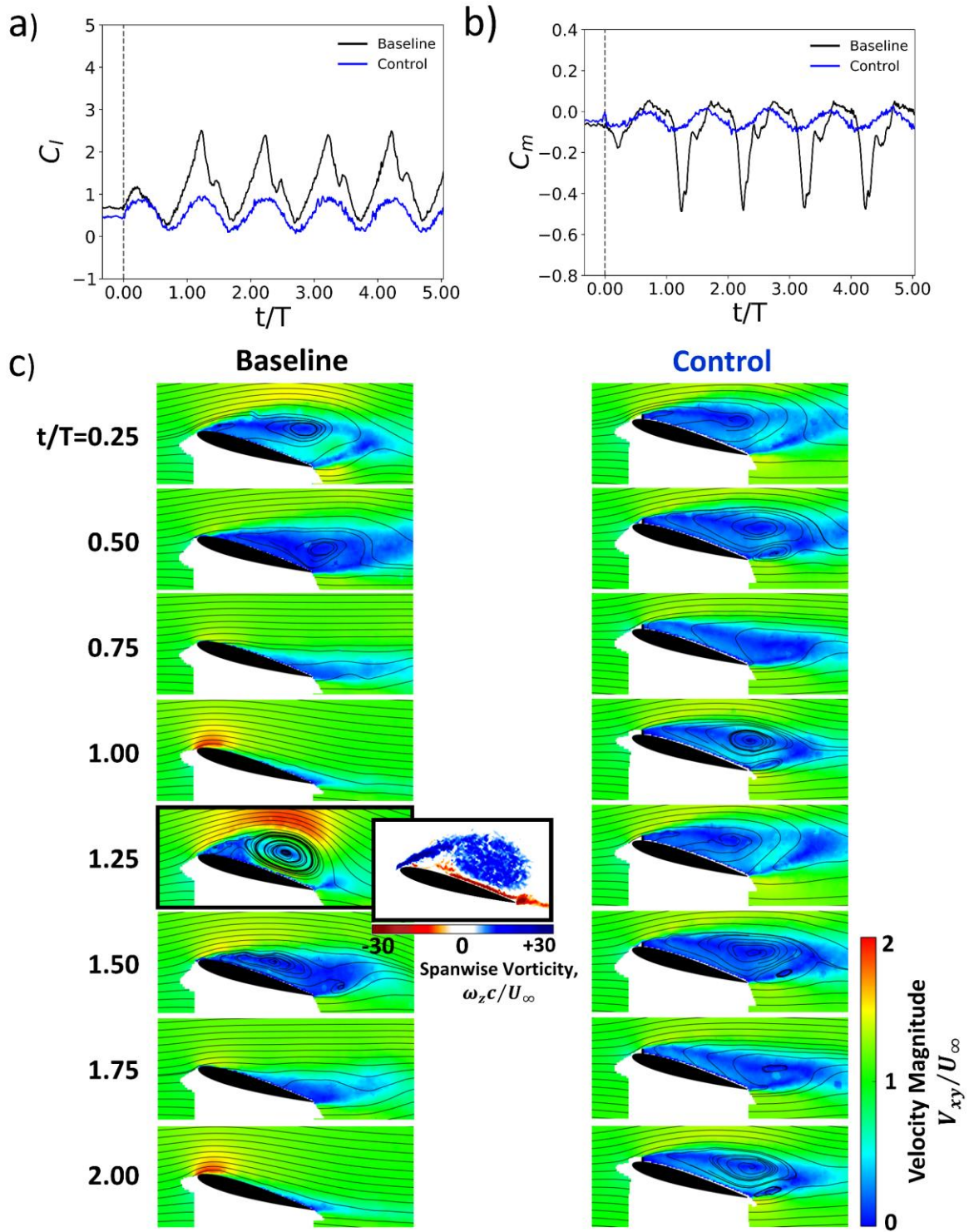**Figure 16:** Transient lift (left column) and pitching moment (right column) performance, *A/c*=0.5.

**Figure 17:** Transient a) lift coefficient, b) pitching moment coefficient, c) normalized velocity magnitude with streamlines, $\alpha_0$=15º, $A/c$=0.5, $k$=0.24.